FNAL Proposal No. 683
Scientific Spokesman
L.R. Cormell
215-243-8551
312-840-4206

PHOTOPRODUCTION OF HIGH P_t JETS

M. Arenton, W.R. Ditzler, T. Fields, R. Stanek
Argonne National Laboratory, Argonne, IL 60439

M. Dris, G. Grammatikakis, E. Simopoulou, A. Vayaki
NRC Democritos, Athens, Greece

J. Butler, M. Harrison
Fermilab, Batavia, IL 60510

A. Kanofsky
Lehigh University, Bethlehem, PA 18015

J. Cooper, L.R. Cormell, C. Hitzman, W. Kononenko, B. Robinson,
W. Selove, G. Theodosiou, B.T. Yost
University of Pennsylvania, Philadelphia, PA 19104

M. Corcoran, H. Miettenen, G.C. Phillips, J. Roberts
Rice University, Houston, TX 77001

A.R. Erwin, M. Thompson
University of Wisconsin, Madison, WI 53706

Photoproduction of High P_t Jets

In this experiment we will study the photoproduction of high p_t jets in the new Wide Band Beam of the Tevatron. The objectives of this experiment are to observe photoproduced jets, to separate three jet from four jet events, to measure the differential cross-sections as functions of p_t, x_t and y, to compare the data with the QCD predictions, to measure the photon structure function, to measure the gluon structure function of the proton, and to study quark and gluon jet properties.

The study of interactions at large transverse momentum from ep, μp, pp and πp collisions has provided valuable information concerning hadron structure and dynamics. Notably absent from this list is the study of high p_t interactions produced by real photons. Because of the point-like coupling of the photon to quarks, the photon is a unique probe of hadron structure and should provide a relatively "clean" interpretation of the interactions.

In QCD two types of photon induced high p_t interactions are possible: (1) the photon could couple directly to a quark in the target transfering all of its momentum to the sub-process interaction, or (2) the photon could disassociate into a virtual quark, anti-quark pair and then one of the quarks in this pair could interact with a parton in the target proton. The first of these interactions would give rise to a three jet event structure. There would be two high p_t jets and one backward (cm) "target jet". The second of these interactions would have a four jet event structure where a fourth jet, in addition to the three jets described above, would be produced as a "beam jet" by the "spectator" quark of the virtual pair. The characteristic signature of the three jet events would be the absence of a beam jet and the fact that the energy of the photon in the lab would equal the energy of the two high p_t jets in the lab.

We propose the addition of a photon momentum tagging system to the Wide Band Beam. Photons in the momentum range of 200 to 600 GeV/c will be tagged with a momentum uncertainty of ≃2%. Photon tagging will be necessary to separate the three jet from four jet events.

A plan view of the apparatus is shown in figure 4.1. It consists of wide-angle magnetic spectrometer, two large calorimeter arrays, and two ring imaging Cerenkov detectors. The spectrometer will be comprised of an SCM-105 magnet and 20 planes of drift chambers and PWC's. The hadron portion of the calorimeter will be segmented in area and depth and will contain 708 modules. The electromagnetic portion of the calorimeter is designed to provide good position resolution for showers. The upstream Cerenkov detector will separate π/K/p in the momentum range of 14-40 GeV/c while the downstream detector is designed to separate π/K/p in the momentum range of 40-130 GeV/c.

About half of the apparatus for this experiment already exists as part of E-609. The new equipment will cost about $1M and can be constructed in about 2-3 years which is consistent with the construction schedule for the new Wide Band Beam. The running time requested is 1500 hours which will be divided into a period of about 500 hours for equipment calibration and some hadron beam running and a period of about 1000 hours for data runs with the photon beam.

Photoproduction of High P_t Jets

Preface

We are presenting in this proposal a systematic list of physics goals and objectives that will be obtainable in the new Wide Band Photon Beam at the Tevatron. While all of these objectives are of current topical interest, it is quite possible that some of these goals will have been met by other photoproduction experiments by the time that this proposed experiment could be conducted. On the other hand, it surely will be of interest to conduct such experiments at Tevatron energies for several reasons:

1. Jets of higher p_t are more easily measured,
2. Theoretical calculations are more reliable at higher energy,
3. Deviations from expected scaling behavior may be found,
4. The lower energy experiments may not yield sufficiently detailed information, and finally,
5. Unexpected results may be found.

These reasons are discussed in more detail in the proposal that follows.

For completeness, we discuss these reasons briefly here. It is fairly well known from the first generation experiments studying jet production that measurement of jets in the 3-5 GeV/c range of p_t is rather difficult. However, the indications from PETRA are that jets of higher energy are more readily recognized and measured. We expect a similar improvement at the Tevatron where jets of up to 10 GeV/c in p_t will be produced. Not only will the experimental measurement become easier but the reliability of the QCD predictions becomes greater at higher energy. At large p_t the calculations will be much less sensitive to smearing effects and corrections from higher twist diagrams.

There is presently one proposed jet photoproduction experiment at CERN. If it is approved, we expect that the CERN experiment will provide useful information at lower p_t, but will probably suffer many of the difficulties that have been experienced in the first generation hadron jet experiments. Besides the difficulties associated with the measurement of low p_t jets, an experiment at CERN will also suffer a rate limitation at high p_t in a lower energy photon beam. The Tevatron Wide Band Beam as proposed will provide a flux of $1x10^6$ photons of energy greater than 500 GeV per spill. This high energy, high flux beam will enable us to measure jet production in the range of 6-8 GeV/c where we expect to test QCD quantitatively.

Finally, we feel that the last item above deserves some consideration at least philosophically. At present the theoretical descriptions of electro-weak and perhaps strong interactions are believed to be understood in terms of the neat and tidy packages of the minimal (SU(2)xU(1) model and QCD. Perhaps even a grand unification of all three forces exists. This simplified view, if taken to the extreme, would leave the experimental physicist with nothing to do except measure the lifetime of the proton and to clean up a few missing measurements. We reject this opinion quite strongly by citing the two most recent Nobel prizes awarded in high energy experimental physics. The discovery of the J/Psi was an almost totally unexpected and certainly revolutionary discovery. Secondly, the discovery of CP violation in the decay of K mesons would not have occured if rare decays had not been searched for and studied. Consequently, we feel it is necessary to expect the unexpected and to be in a position to study such developments. We are thus led to construct a multi-purpose, flexible

detector with sufficient versatility and analysis capabilities to exploit such possibilities, particularly since the same detector can be used to answer several physics questions with both hadron and photon beams.

1. Introduction

The study of interactions at large transverse momentum has proved to be a fruitful source of physics results in essentially every type of interaction -- ep, μp, pp, πp. Notably missing from this list is the study of γp interactions at high p_t with real photons. Considering the insights of hadron structure and dynamics which has been provided by deep inelastic scattering (DIS) and high p_t hadronic measurements and the uniqueness of the photon as a probe of hadronic structure, we feel it is imperative that high p_t photo-production experiments be conducted -- especially at the Tevatron.

The unique coupling of the photon to quarks provides a "cleanliness" to the interpretation of photon interactions when compared to hadron interactions. Consequently, the results, both experimentally and theoretically should be easier to extract. A further important advantage is gained at Tevatron energies where jets of higher p_t are produced. We illustrate this situation in figure 1.1 where we have shown typical interactions at p_t = 4 and 8 GeV/c for both photon and hadron interactions. In figure 1.1a, a typical jet interaction in the γp center of mass is shown. This event at $\sqrt{s}$ = 19.4 GeV is dramatically different from the event in figure 1.1b at $\sqrt{s}$ = 30.6 GeV and p_t = 8 GeV/c. In much the same way that jets at PETRA have been observed in a spectacular way as compared to SPEAR jets, jets at the Tevatron will be very easily observed as compared to lower energies where jets are observed essentially at "threshold". Finally we compare these two events with the hadronic interactions in

figure 1.1c and 1.1d where the problem of unscrambling the beam jet fragments from the high p_t jets adds a further complication not present in the photoproduced jets. This spectacular feature, and probably the most important experimental feature of jet photoproduction, is simply due to the fact that all of the photon energy in a three jet interaction is transferred to the sub-process interaction. We note in passing that even for the hadronic production of jets, the increase in energy available at the Tevatron improves the recognition of the high p_t jets. We will discuss the advantages of jet photoproduction at the Tevatron in further detail in the next section.

We expect to exploit this simplified event topology and the pointlike coupling of the photon to investigate hadron structure, to study quark and gluon fragmentation, and to quantitatively test QCD.

As mentioned above, the photon transfers all of its energy to the high p_t interaction. This means that the total energy of the high p_t jets in the lab will equal the energy of the photon. To take advantage of this remarkable property will require a photon tagging system. We will describe in a later section how such a system could be added to the proposed Wide Band Beam to provide tagging with an accuracy of a few percent. This relatively small addition to the proposed beam line will supply the final ingredient necessary to augment the Wide Band Beam's distinct advantages in energy and intensity.

The apparatus necessary to carry out this study of high p_t photoproduction is large in scale but certainly not beyond the realm of present large scale spectrometers at Fermilab. Much of the apparatus already exists as part of E-609. In fact the present E-609 spectrometer could be used as is for a first look while the additional equipment was being brought

"on-line". Furthermore, much of this proposed apparatus would be used in our proposed experiment "Jet Production in 1000 GeV Hadron Collisions". The versatility of the Wide Band Beam would be more fully utilized by alternately running both photon and hadron experiments. For a very small investment of protons one can study high p_t hadronic interactions in the same apparatus to be used for the study of jet photoproduction.

2. Physics Objectives

The foremost objective of this experiment will be the convincing observation of photoproduced jets. The properties and distributions of these jets will be studied. We state the particular measurements we hope to make in the following list. In the remainder of this section, we describe the feasibility of attaining these goals, their importance, the expected production rates, backgrounds, and the advantages of high p_t photoproduction.

Objectives of this experiment:

1. Observation of photoproduced jets
2. Separation of 3-jet and 4-jet events
3. Cross-section measurements as functions of p_t, x_t, and y
4. Comparison of the data with QCD predictions
5. Measurement of the photon structure function
6. Measurement of the gluon structure function of the proton
7. Study of quark and gluon jet properties

From DIS results and low p_t photoproduction we expect the three types of interactions shown in figure 2.1 to give rise to high p_t jets. These diagrams are calculated in first order QCD or by vector meson dominance (VMD).

2.1 Three jet events

The two diagrams in figure 2.1a are usually referred to as the QCD Compton and the photon-gluon fusion diagrams respectively,[1] and can be calculated exactly in first order QCD. There are several attractive reasons for

studying interactions of this type:

1. The photon-quark coupling is pointlike .
2. The photon transfers all of its energy to the interaction .
3. There is no beam jet.

Consequently, this reaction is more easily measured and calculated. There will be only three jets in the final state -- two at high p_t and a backward (cm) target jet. This topology presents a tremendous simplification over hadronic interactions as shown in figure 1.1c and 1.1d where the beam jet becomes a background source of particles which are somewhat difficult to identify. The feature which uniquely identifies these three jet events is the fact that the lab energy of the photon, E_γ , is approximately equal to the sum of the lab energies of the two jets:

$$E_\gamma = E_1 + E_2 \tag{1}$$

Furthermore, if the momentum and direction of one jet is measured, the momentum and direction of the second jet can be calculated (Note that this calculation assumes that there is no smearing from parton internal transverse momentum, K_t).

$$p_t = p_{t1} = p_{t2} \tag{2a}$$

$$p_t = E_1 \sin\theta_1 = E_2 \sin\theta_2 \tag{2b}$$

$$\sin\theta_2 = \frac{E_1}{E_2} \sin\theta_1 = \left(\frac{E_1}{E_\gamma - E_1}\right) \sin\theta_1 \tag{2c}$$

Because of this kinematic relationship these three jet events will present a unique signature when compared to the four jet events produced by the interactions pictured in the diagrams of figure 2.1b and 2.1c. Photon momentum tagging will be required in order to make use of equation (1).

2.2 Four jet events

Since the photon couples directly to all quark pairs in proportion to the quark charge squared, interactions of the type shown in figure 2.1b will also be produced. These events will have the characteristic four jet structure as is observed in hadronic interactions. Two jets are produced at large p_t from the interacting partons and the spectator partons form beam and target jets. These events will not produce jets of the highest p_t as in the three jet case and can be separated on a kinematic basis as described above. While these four jet events are perhaps not as spectacular as the three jet events, they are of interest to measure for at least two reasons: (1) All of the subprocesses predicted by QCD for high p_t hadronic interactions will contribute to these scatterings, and (2) the photon structure function is expected to be peaked toward large x.[2] By measuring these events we will be able to study strong interaction subprocesses if the photon structure function is known or conversely by comparing these interactions to the hadronic measurements (e.g. E-609) we will be able to determine the photon structure function. This possibility becomes particularly attractive if some data can be taken with hadrons incident using exactly the same apparatus.

2.3 Vector meson dominance

A second type of four jet event will be produced by VMD. This type of interaction is shown in figure 2.1c where the photon has coupled to a vector meson - ρ, ω, ϕ . The contribution from this class of events has been calculated to be small at moderate to large p_t.[3] Experimentally

it will be indistinguishable from the four jet events described above. Consequently these VMD events will provide a small contribution to the photon structure function.

2.4 Separation of three jet from four jet events

Many of the physics results we hope to obtain in this experiment are dependent on the ability of the apparatus to resolve three jet from four jet events. The degree to which we can separate these classes of events involves detailed questions of the relative cross-sections, the energy resolution of the beam, and both the angular resolution and energy resolution of the jets. (See equations (1) and (2).) We discuss these questions individually in later sections of the proposal. In this section, however, we will consider their collective effect on the separation of these two classes of events.

Because of the relation described by equation (1), only the three jet events are found at the kinematic limit $x_c = 1$, where

$$x_c \equiv \left(\frac{E_1 + E_2}{E_\gamma}\right) \qquad (3)$$

This kinematic boundary will be smeared by the experimental resolution, so that some four jet events will appear in the three jet bin. Similarly, if events at fixed p_t, fixed $\sqrt{s}$, and fixed θ_1 are plotted vs. θ_2, the three jet events will appear at an angle given by equation (2). We have calculated the resolution of the detector to a reasonable approximation by Monte Carlo technique[4] for this second type of plot. The result is shown in figure 2.2 where the cross-sections were obtained from reference 3.

Only the calorimeter was used in determining the energy and angle of the jets. Some improvement is possible by using the magnetic spectrometer information in addition. In any event, we estimate that the separation of three jet from four jet events should have a signal to background ratio of at least 5 or 10 to 1. With a separation at this level, the measurement of the relative cross-sections should present no problem and a relatively pure sample of three jet events will be obtained at the kinematic limit.

2.5 Cross-sections

Cross-sections for the contributions to jet photoproduction for the diagrams in figure 2.1 have been calculated by J. F. Owens.[3] We will briefly discuss the input to and the results of those calculations. Basically, the differential cross-section for the production of two high p_t jets, j_1 and j_2, at rapidities y_1 and y_2 is determined by a sum over the product of structure functions, G(x), for each of the interacting particles times the scattering cross-section for each of the diagrams in figure 2.1. That is,

$$\frac{d\sigma}{dy_1 dy_2 dp_t^2}(\gamma p \to j_1 + j_2 + x) = \sum_{a,b} x_a G_{a/\gamma}(x_a) x_b G_{b/p}(x_b) \times \frac{d\sigma}{d\hat{t}}(ab \to j_1 + j_2) \tag{4}$$

where $x_{a/b}$ denotes the Feynman x of the interacting partons (quarks, gluons, photons) in the beam/target, and $\hat{t}$ is the momentum transfer squared (Mandelstam variable) in the parton-parton frame. The scattering cross-sections $d\sigma/d\hat{t}$ are calculated in first order QCD.

For the three jet process there are two terms:

$$\frac{d\sigma}{d\hat{t}}(\gamma q_i \to g q_i) = -\frac{\pi\alpha\alpha_s}{s^2} e_i^2 \frac{8}{3}\left(\frac{\hat{u}}{\hat{s}} + \frac{\hat{s}}{\hat{u}}\right) \tag{5a}$$

$$\frac{d\sigma}{d\hat{t}}(\gamma g \to q_i \bar{q}_i) = \frac{\pi\alpha\alpha_s}{s^2} e_i^2 \left(\frac{\hat{u}}{\hat{t}} + \frac{\hat{t}}{\hat{u}}\right) \tag{5b}$$

where $\hat{s}$, $\hat{t}$, and $\hat{u}$ are the Mandelstam variables in the parton-parton frame and e_i is the fractional charge of the i'th quark. In these calculations the momentum transfer squared between the photon and the outgoing quark q_i is defined as $\hat{u}$. Consequently, $\hat{t}$ is the momentum transfer squared between the photon and the outgoing gluon in (5a) and between the photon and the outgoing anti-quark $\bar{q}_i$ in (5b). We can express the angular dependence of these equations in terms of the scattering angle $\hat{\theta}$ in the parton-parton cm frame:

$$\gamma q_i \to g q_i : \left(\frac{\hat{u}}{\hat{s}} + \frac{\hat{s}}{\hat{u}}\right) = 1 + \tan^2\hat{\theta}/2 + \cos^2\hat{\theta}/2 \tag{6a}$$

$$\gamma g \to q_i \bar{q}_i : \left(\frac{\hat{u}}{\hat{t}} + \frac{\hat{t}}{\hat{u}}\right) = \tan^2\hat{\theta}/2 + \cot^2\hat{\theta}/2 \tag{6b}$$

where $\hat{\theta}$ is the angle between the photon and the outgoing gluon in (6a) and between the photon and the outgoing anti-quark $\bar{q}_i$ in (6b). We see that these equations have a rather similar $\hat{\theta}$ dependence for the outgoing quark predicting a forward peak in $\hat{\theta}$ in either case. The $\hat{\theta}$ angular distribution for the outgoing gluon, however, in (6a), is quite different. There is a backward peak for the outgoing gluons.

The actual experimental differential cross-section for two high p_t jets, (4), depends on the product of $d\sigma/d\hat{t}$ and the structure functions. We thus see that the separation of processes (5a) and (5b) will be facilitated by taking data at a suitably chosen x_b. One has the possibility of

obtaining a sample of three jet events relatively rich in the qg final state by selecting a data sample at relatively large x_b since $G_{q/p}(x_b) >> G_{g/p}(x_b)$ at large x_b. Moreover, for such events, if one examines the data region in which one of the high p_t jets is observed at a $\hat{\theta}$ value appreciably forward of 90^o, then that jet is most likely to be a quark jet and the other high p_t jet is most likely to be a gluon jet. We hope to make use of these effects to study relatively pure samples of quark jets and gluon jets. Also since the coupling is proportional to e_i^2, the scattering is primarily from up quarks by a factor of about 8 to 1 in the proton -- so in particular, we will be studying u quark scattering and fragmentation.

The four jet interactions will contain all of the scattering subprocesses that occur in hadron-hadron collisions, i.e. qq→qq, qg→qg, ... These cross-sections have been calculated by several authors[5,6,7]. The proton structure functions are taken from extrapolations of lepton scattering data[7,8] and the photon structure function is calculated in the QCD leading log approximation[2,3,9]. The photon structure function is shown in figure 2.3 as predicted by the QCD leading log approximation along with a VMD estimate for the structure functon.

The predictions for each of the subprocesses in figure 2.1a and 2.1b are shown in figure 2.4 for $\sqrt{s}$ = 19.4 GeV. At low p_t the four jet terms dominate, but at large p_t the three jet events - in particular those events produced by QCD Compton scattering - dominate. The total first order QCD prediction for jet photoproduction is plotted again in figure 2.5 along with the VMD contribution and a comparison to hadron jet production at $\sqrt{s}$ = 19.4 GeV as measured by E-395.[10,11] The predicted cross-sections at 90^o for $\sqrt{s}$ = 19.4, 27.4 and 30.6 GeV are shown in

figure 2.6. The vector dominance contribution is expected to be small at large p_t. The QCD jet photoproduction, on the other hand, is predicted to be larger than the hadron jet production at high p_t. This is mainly due to the fact that the photon contributes much (all) of its energy to the highest p_t four jet (three jet) interactions whereas hadrons can only contribute some fraction, x, to the subprocess. Another way of stating this expectation is that the photon contains a significant component both at large x (hadron-like coupling in figure 2.1b) and at x = 1 (point-like coupling in figure 2.1a), while hadron structure functions fall off rapidly ~ $(1 - x)^m$, where $m \simeq 3$ (1) for protons (pions).

Another reflection of the photon's structure and coupling is a slower p_t dependence of the cross-sections. While the basic QCD processes predict $1/p_t^4$ for either hadron or photon production, the hadronic production of single particles in this p_t range is proportional to $1/p_t^8$. This sharpening of the p_t dependence as described by QCD arises from several sources: scale violation in the coupling constant $\alpha_s(Q^2)$, scale violations in the structure functions, and K_t smearing.[7,8] The p_t dependence of jet photoproduction is expected to be less steep ~ $1/p_t^{4-6}$. This is because there should be a smaller effect from K_t smearing and the product of $\alpha_s(Q^2)G_{a/\gamma}(x,Q^2)$ scale for both quarks and gluons[3].

2.6 Rates

We defer the detailed discussion of beam flux and interaction rate to the next section, but we summarize that discussion by quoting the achievable cross-section sensitivity here. In figure 2.5 we have also shown the cross-section level corresponding to 1 event/hour for a Wide Band Beam electron setting of 450 GeV/c and a liquid hydrogen target of 45 cm length. So in a 100 hour run usable statistics would be obtained for events with p_t out to 6 GeV/c at 200 GeV/c. At this level, the

QCD prediction indicates that the high p_t interactions will be dominated by the three jet events.

2.7 P_t dependence

As discussed above the p_t dependence of jet photoproduction is expected to be less steep than hadron jet production. Also the p_t dependence is likely to be different for the three jet and four jet events. The measurement of the $1/p_t^n$ dependence is done by comparing the production at fixed $x_t = 2p_t/\sqrt{s}$ and fixed θ^* for different values of s. If the cross-section scales, one obtains a unique value for n in the following way. The cross-section can be paramatrized as

$$\sigma_{inv}(s) \equiv E\frac{d^3\sigma}{dp^3} \sim f(x_t,\theta^*)\ \frac{1}{p_t^n} \qquad (6)$$

Then by taking the ratio of cross-sections at fixed x_t and θ but different beam momenta the n dependence can be found:

$$\frac{\sigma_{inv}(s_1)}{\sigma_{inv}(s_2)} = \frac{p_t(s_2)}{p_t(s_1)}^n = \left(\frac{s_2}{s_1}\right)^{n/2} \qquad (7)$$

In hadron jet experiments this measurement requires taking data at several beam momenta. In jet photoproduction a large range of beam momenta are available simultaneously. In QCD the value of n is not expected to be unique because of scaling violations. Nevertheless, a measurement of n in jet photoproduction which gave a value less than n = 8 as typically observed in this p_t range for hadron production would be a confirmation of this aspect of QCD.

2.8 K_t smearing

The effect of K_t smearing in hadron jet production increases the steepness of the p_t fall off by about two powers of p_t.[7] The K_t smearing has this effect on the p_t dependence mainly because of the trigger bias it introduces when only one jet is measured. The magnitude of this effect can be reduced by triggering on the sum of p_t in the two high p_t jets[8,12,13]. A similar situation occurs in jet photoproduction -- but the magnitude of the K_t should be smaller for the three jet events. In the three jet events the photon couples directly to the scattered quarks, so the only source of internal transverse momentum is the proton target. In the four jet events the photon first produces a virtual pair of quarks before scattering, so the situation is different. Thus the magnitude of K_t, seen as an unbalance of p_t values between the two high p_t jets, should be different for the three jet and four jet events.

2.9 Photon structure function

In the QCD phenomenology as described above the jet photoproduction cross-section is proportional to the photon and proton structure functions for the four jet events. The jet cross-sections for incident hadron beams are calculated in the same way in QCD with the same scattering subprocesses and the same proton structure function. So by taking the ratio of cross-sections of jet photoproduction to hadron jet production at the same s, and at x_a (beam) values above 0.25 to 0.3 or so, where the valence quark structure functions should dominate over other parton species in the hadron, one can obtain an approximate quark structure function for the photon. This is the same method that was used to measure the pion structure function in E-395[14]. Taking ratios of cross-sections to determine the structure function eliminates the problem of properly normalizing the result. Thus it is imperative that

hadron jet measurements be done with the same apparatus to minimize the systematic errors in taking this ratio.

2.10 Subprocess scattering cross-section -- test of QCD

A direct test of the QCD prediction of the subprocess scattering cross-section (eq. 5) can be made in the three jet events. In these events the photon couples directly to the interacting partons via the diagrams in figure 2.1a. Consequently, the measured result should depend only on the structure function of the proton and the QCD prediction of the subprocess interaction. These two diagrams involve both the quark and gluon distributions of the proton. The gluon distribution function in the proton has not been measured well[7,8], but the u quark distribution ($F_2(x, Q^2)$) of the proton is extremely well known[15]. It is possible to independently study the interaction $\gamma q \to gq$ where only the QCD scattering cross-section has not been measured. These QCD Compton interactions dominate the jet production at large p_t, $x_t > 0.4$ as seen in figure 2.4. By studying these events, the subprocess scattering cross-section, $d\sigma/d\hat{t}$, can be extracted and directly compared to the QCD prediction. These interactions have a particular advantage in the cleanliness of their interpretation. There is only one diagram in first order QCD -- the theory can be pinned down in a way not possible in most interactions.

The remainder of the three jet interactions, $\gamma g \to q\bar{q}$ which dominate at small x_b can also be studied independently. These events will depend on the proton gluon distribution. More refined measurements of the gluon structure function are likely to be made during the next few years; e.g. a way of making this measurement is suggested in reference 16. So again we will be able to directly measure a particular subprocess scattering and to compare it to the QCD prediction; or conversely if

the QCD prediction is assumed to be correct, we can extract a measurement of the gluon distribution in the proton.

2.11 Gluon and quark jet fragmentation

It has been a long standing goal of jet epxeriments to obtain information on the properties of gluon jets as compared to quark jets. The basic problem, thus far, has been that no gross differences are apparent in the jets that have been studied. In fact the only direct evidence that gluon jets exist comes from PETRA. In hadron jet experiments many competing subprocesses involving quarks and gluons are involved, so it is difficult to find kinematic regions where a particular species can be separated or at least enhanced.

An exception to this difficulty is found in the hadron production of direct photons and jets as described in ref. 16. An analogous situation occurs in the three jet events as shown in figure 2.1a. In the case of the γg fusion diagram a q jet and a $\bar{q}$ jet are produced at high p_t. Since the gluon distribution is concentrated at low x while the photon couples at $x = 1$, the γg subprocess and the two high p_t jets produced are moving forward in the cm. This effect shows itself also in the θ^* and p_t distributions for inclusive single jets at high p_t. In this case the ratio of gluon jets to quark jets is also affected by the fact that gluon jets, from γq scattering, tend to go backwards in $\hat{\theta}$ as discussed in section 2.5. The net effect is illustrated in figure 2.7 for the angular dependence of the ratio R_g, defined by

$$R_g = n_g/(n_g + n_q)$$

where n_q (n_g) is the number of quark (gluon) jet triggers. This prediction from reference 3 indicates that the number of gluon jets produced at forward angles falls off rapidly.

Consequently, quark jets (and in particular u quark jets, because of the factor e_i^2 in equation (5)) can be studied in a forward calorimeter. These jets could be studied independently and an identification scheme based e.g. on the π^+/π^- ratio for the leading particle in the jet could be explored. Then by studying the three jet events in other kinematic regions where gluon jets are enhanced, some of the quark jets could be tagged and a detailed study of gluon jets could be made. Gluon jets should be totally neutral in all additive quantum numbers and should couple with equal strength to all quark pairs. Consequently, an identification of K mesons, for example, in the jets may provide a good tag of gluon jets. Such an identification will require sophisticated Cerenkov devices such as the type we describe in section 4.

3. Wide Band Beam and Tagging System

The wide band beam as proposed for the Tevatron is described in detail in reference 17. This proposed beam presents several advantages over existing photon beams -- intensity and energy being the most important. An additional advantage of the beam line is the fact that hadron beams will also be available. The addition we are proposing to this beam line is a photon tagging system that will determine the photon momentum to $\simeq$ 2%. The additional equipment described here is modest in cost and complexity in comparison to the beam line as a whole. We feel that this small investment is well worth the increased physics capabilities.

3.1 Beam line

The optics of this beam line are shown in figure 3.1. The beam is quite versatile and can be run in several modes -- diffracted proton beam, pion beam, neutral beam or electron/photon beam. The beam line is designed as a two stage system with a very large acceptance in momentum and solid angle. Consequently, the beam can transport large fluxes of particles. The particle yields for pions and electrons are shown in figures 3.2 and 3.3

The electron beam is produced by converting photons from π^o's downstream of the production target. The primary protons are dumped just downstream of the target box, a 0^o neutral beam is formed at the target box, photons are converted to electrons, the electrons are bent away from the 0 degree beam and transported through the beam optics to the bremsstrahlung target. The unconverted photons, neutrons, and K^o's are dumped at the momentum collimator.

The Wide Band Photon Beam so produced has several distinct advantages: 1) The photon energy will be the highest available in the world; 2) the intensity is quite large; and 3) the hadron background will be quite small. This first advantage is obvious and has been discussed in section 2. We now turn to a discussion of the other advantages.

3.2 Photon flux and event rates

Because of the large momentum acceptance of the beam line ($\pm$15%), a large photon flux is possible. This flux is shown in figure 3.4 for 450 and 600 GeV/c electron beams. We consider some specific examples in table 1. For a 10% photon momentum bite the flux is typically 10^6 photons which will permit studies of interactions in the range of 100 pico-barns for the differential cross-section. In table 2 we compare the presently existing photon beams with the new Wide Band Beam and the FNAL Tagged Photon Beam at 1 TeV. The Wide Band Beam's high intensity at high energy is unsurpassed by the other bremsstrahlung beams and the background levels as we describe below are substantially lower than in the present Broad Band Beam.

In table 3 we indicate the event rates for $\gamma p \rightarrow$ jet + x at 90° for several beam energies as a function of p_t. We have assumed a run of 100 hours (6000 pulses at 10^{12} protons/pulse), a 45 cm liquid hydrogen target and a solid angle of 1 ster-radian at 90°. Relatively high statistics are obtained for p_t's of 5 at 500, 6 at 200 and 7 GeV/c at 400 GeV/c in such a run. The highest p_t obtainable at the 1 event level will be about 10 GeV/c at 400 GeV/c corresponding to a differential cross-section of about

2 pico-barns. An even higher sensitivity will be obtained at angles more forward than 90^{o} where the cross-section increases by a factor of 5-10 at high p_t. At these high p_t's the interactions will be dominated by the QCD Compton scattering as described above.

3.3 Muon and hadron backgrounds

The muon background in the Wide Band Beam experimental hall will be about a factor of 20 lower than the projected rate at 1 TeV/c for the present Broad Band beam. This background originates from the decay of π's generated in the primary production target and from prompt muon production in the target, the proton dump, and the neutral dump. These backgrounds have been calculated by Monte Carlo generation.[17]

We summarize those calculations as applied to our proposed detector in figure 4.1. The integrated flux over the detector will be approximately 6×10^{6} muons per 10^{12} protons on target. These muons if not vetoed can produce high energy delta rays in the calorimeter which could become a troublesome source of spurious signal. However with a muon anti-counter wall these muons can be vetoed to the 98% level. The counting rate per muon anti-counter (50 cm x 200 cm) will be a tolerable 10^{6} per 10^{12} protons in a 10-20 second spill. In addition to the muon anti-counter wall just upstream of the detector several more anti-counters are placed around the bremsstrahlung radiator as shown in figure 3.5. These anti-counters would be used to help veto hadronic interactions, beam halo, tridents, and secondary photon interactions in the radiator.

Even with a muon anti-counter array the spurious p_t produced by delta rays can have a serious effect for the case of single-arm triggers (trigger on one high p_t jet). For the case of double-arm triggers (trigger on the sum of p_t on both sides of the beam), however, the effect of delta rays becomes negligible. The delta ray background could also be reduced to a negligible level for the single-arm triggers by the addition of a second muon anti-counter plane with an additional rejection factor of 50.

One of the most serious problems for the present Broad Band Beam is the neutral hadron background. This background will be reduced by about two orders of magnitude in the new beam line. The source of this background in the new beam originates in the production of π^-'s by neutrons in the lead converter. Some of these pions are accepted by the electron beam transport and strike the downstream radiator. A small fraction of these pions interact in the radiator producing forward neutrons and K^o's which ultimately reach the experimental target.

Calculations for this background are presented in reference 17. The ratio of π^-/e^- at the radiator is predicted to the 4%. The radiator will be 30% of a radiation length corresponding to 1% of an absorption length in lead. Consequently, the ratio of interacting hadrons to photons will be $\approx 1.3 \times 10^{-3}$ and only about 1% of these interacting hadrons will produce forward going neutrons or K^o's. At the experimental target, then, the hadronic background will be less than 1.3×10^{-5}. The ratio of hadronic interactions to photon-produced hadronic final states will be less than 3.5×10^{-3} for a 45 cm liquid hydrogen target.

3.3 Tagging system

To fully utilize the advantages of the new Wide Band Beam it is imperative that a photon tagging system be added to the bremsstrahlung beam. As described in section 2, we will be able to identify the three jet events (which have considerable significance in their production and interpretation), if the photon momentum is known. The system we have designed will be constructed using conventional detector techniques (drift chambers and Pb/scintillator shower detectors) and will tag about 25% of the photons produced with energy greater than 25 GeV. Essentially all photons of energy greater than 200 (300) GeV at 450 (600) GeV/c will be tagged) with a measurement uncertainty of about 2%.

The tagging is accomplished by performing three separate measurements: (1) measurement of the initial electron momentum; (2) measurement of the final electron momentum; and (3) measurement of the photon direction. The difference between the measurements (2) and (1) determines the photon energy. Measurement (3) and its importance are discussed below. The system is shown in figures 3.5 and 3.6.

The upstream end of the tagging system will determine the initial electron momentum. It consists of three narrow cell drift chambers located at the final bend string, B3. Each chamber will contain 100 wires with 1 mm spacing and should measure the electron position to about 200 microns. The planes are separated by about 3 m, so the angular resolution of the bend angle should be 0.1 mr. The magnets are operated at 1.6 Tesla, so the momentum resolution for the electron beam should be 1.4% at 450 GeV/c and 1.9% at 600 GeV/c.

The downstream end will measure the electron's energy after it has emitted a bremsstrahlung photon. The "C" magnet will sweep the electrons away from the photon beam and into the shower detectors. The electron shower detectors will be 10 cm x 10 cm x 24 X_o Pb /scintillator

sandwiches. Eight counters will be placed 20 m from the radiator and another eight at 10 m in such a way that photons in the range of 300-570 GeV will be tagged with 600 GeV/c electrons incident. By rearranging the detectors, photons in the range of 200-420 GeV/c can be tagged for a 450 GeV/c electron run. The average energy resolution and counting rates for each detector are summarized in table 4. The energy resolution of the Pb/scintillator detectors will be better than the energy resolution for the initial electron energy. Further improvement in the measurement accuracy of the photon energy is not required since the error in the measurement of

$$E_\gamma = E_1 + E_2$$

will be dominated by uncertainties in the measurement of the energies of the two jets.

The measurement of the photon direction is also necessary to determine the amount of momentum it carries transverse to the nominal beam center. This transverse momentum, call it p_t(beam), will smear the p_t unbalance of the two high p_t jets. As described above, we would like to measure the amount of K_t associated with the scattering quarks and gluons. Systematic, but calculable, contributions to the K_t measurement will come from the energy resolution of the calorimeter[12,13] and from p_t(beam).

A second effect caused by p_t(beam) is the introduction of a trigger bias in the single jet triggers. Jets produced by photons moving toward the trigger side will register in the detector as jets of higher p_t than their actual true p_t. This effect can also be corrected for if the direction and momentum of the photon is known.

The divergence of the photon beam is about 0.6 mr, so p_t(beam) could be as large as 300 MeV/c. We propose to reduce the magnitude of

this effect by determining the photon direction to an accuracy of better than 0.2 mr. This measurement will reduce the uncertainty in p_t(beam) to less than 100 MeV/c. The direction of the photon will be determined by measuring the position of the electron at the Pb radiator with a 1 mm crossed hodoscope (figure 3.6) and by locating the interaction vertex in the target to within a few millimeters.

4. Apparatus

The apparatus proposed for this experiment is shown in figure 4.1. Most of the elements in this setup are used in another Tevatron proposal being made for the study of hadron jets.[19] Basically, the apparatus consists of a wide angle charged particle spectrometer and two large calorimeter arrays. Of primary importance is the angular coverage of the calorimeter. This coverage is shown in figure 4.2 for $\sqrt{s}$ = 19.4 and 30.6 GeV. The calorimeter array can be moved quite easily to allow the same angular coverage at several energies. This large angular coverage will be necessary to study the angular dependence of the jets and in particular to study the three jet events described above which tend to go more forward in the overall cm. The spectrometer consists of a large aperture magnet, PWC's, and high resolution drift chambers. The magnet is operated at relatively low field, p_t(magnet) $\simeq$ 100 MeV/c, so the p_t of the jet is not considerably distorted. The spectrometer when run in this mode is not designed to provide a high precision momentum resolution. Rather its major functions are: to augment the calorimeter resolution for low momentum tracks, to determine charged particle multiplicity, to determine the sign of the charge of higher momentum tracks, to locate the interaction vertex, and finally in conjunction with the Cerenkov detectors to determine particle identification.

4.1 Calorimeter

The calorimeter is a modular array segmented in area and depth. The upstream faces of the outer (upstream) and inner (downstream) detectors are shown in figures 4.3 and 4.4 respectively. Both the inner and outer calorimeters contain

an electromagnetic detector as the front end followed by 6-8 absorption lengths of iron calorimeter. The iron calorimeter modules consist of iron scintillator sandwiches with BBQ readout as shown in figure 4.5. The outer detector will be constructed from modules used in E-395/609. The inner detector will be constructed of modules of this same type.

The electromagnetic detector will be a refined and improved version of the front layer of the E-609 detector. This detector will have high spatial resolution for separating nearby e-m showers which will allow the separation of single showers from double showers (π^o's) over a large range in energy. The position resolution is obtained from PWC's installed in the detector which sample the shower size and energy after 3 and 6 radiation length as sketched in figure 4.6. While the position information will come from the PWC's, the energy of the e-m showers will be measured by scintillators sandwiched in the lead every 1/2 radiation length.

The energy resolution for jets will mainly be determined by the hadrons in the jets, though the electromagnetic component of the jet will sharpen this resolution by some amount. The existing E-609 calorimeter gives a resolution for hadrons of about $75\%/\sqrt{E}$. The resolution for e-m showers for the proposed detector should be about $15\%/\sqrt{E}$. For jet experiments with rapidly falling p_t distributions, it is well known that the standard deviation of the energy resolution curve of the calorimeter is not the most important consideration. The most important consideration is whether the calorimeter has a high energy "tail" on the energy response

curve caused by some source of spurious signal. The effect of this tail is such that an event of lower p_t will fake one of much rarer high p_t. This effect can become so serious that unfolding the true p_t distribution from the measured may become impossible[20,21]. The E-609 calorimeter does not suffer from such effects[22].

The calorimeter provides the trigger for the experiment. The energy measured is weighted by sin θ, which gives p_t. This p_t measurement is summed over some subgroup of modules to form a trigger. The p_t so measured is then required to be above some adjustable threshold to trigger an event. A typical trigger arrangement is shown in figure 4.7. This trigger is one that would be used to select $\gamma q \rightarrow gq$ three jet events.

4.2 Magnetic spectrometer

The spectrometer, as mentioned above, is designed to aid the calorimeter resolution for low momentum tracks and to help determine particle identification. The magnet must have large aperture to provide the largest angular coverage. A magnet such as the SCM-105 with an aperature of 40 x 84 x 30 inches being used in E-609 is suitable for this purpose. The magnet is run at relatively low field to give a "p_t kick" of only 100 MeV/c. A large field would bend the charged particles too much cauing a smearing of the p_t trigger. The momentum resolution should be

$$\frac{\Delta p}{p} = 0.3\% \; p \; (\text{GeV/c})$$

so that for momentum less than about 30 GeV/c the magnetic spectrometer will have better resolution than the calorimeter.

We are proposing 8 chambers with a total of 20 wire planes for charged particle tracking. Each chamber will contain 2 or 3 PWC or drift chamber planes. The 6 upstream chambers are existing chambers from E-609. The first of these chambers is a PWC containing 3 planes of wires. The remaining five are drift chambers each containing 2 planes of drift wires. Some of the chamber planes have delay line cells which provide a co-ordinated x-y readout. The seventh and eighth chambers will have to be constructed.

4.3 Cerenkov counters

We are proposing to include two imaging Cerenkov counters for particle identification. Just as the calorimeter is divided into inner (downstream) and outer (upstream) detectors, so are the Cerenkov counters. At present the ring imaging techniques look very promising[23,24,25]. Nevertheless, these devices have not been demonstrated to work in a large scale apparatus yet. Should these devices fail to perform as expected, it will still be possible to obtain the physics objectives we have described with a series of segmented threshold Cerenkov counters. We consider this possible "fall-back" option well understood and do not describe such a scheme here.

The major function of the Cerenkov detectors will be the identification of leading charged particles in the jets. Identifying these leading particles should help in the separation of quark jets from gluon jets. That is, a jet with a leading π^+ is likely to have fragmented from a u quark while a leading K^- is more likely to have fragmented from a gluon. For example, the leading particle in the jet at 90^o cm in figure 1.1b would have a lab momentum of about 50 GeV/c and the leading particle in the jet at 40^o cm would have a lab momentum of about 130 GeV/c. The detectors we propose would just be able to separate K^- from π^+ in both cases.

The outer detector will be a ring imaging device known as ORCID (optical readout Cerenkov imaging device)[23]. This device is presently being assembled and will be tested during 1981. The detector elements are shown in figure 4.8. The angular coverage will be from about 25 mr to 200 mr in the lab on each side of the beam. This angular coverage is well matched to the outer calorimeter. The radiating gas in ORCID is Freon 12 which has a high index of refraction ($n - 1 = 1.1 \times 10^{-3}$). This high index of refraction will produce rings with large Cerenkov angles and consequently more photoelectrons in a short radiator than gases with smaller indices of refraction. The Cerenkov light produced in the gas is focussed by two spherical mirrors onto a two stage image intensifier. The image size is reduced by fiber optics coupling and finally the photons are detected by a charge coupled device (CCD).

The ORCID will be capable of measuring the Cerenkov angle to an accuracy of about 0.6 mr. This resolution should give a 3σ $\pi/K/p$ separation in the range of 14-40 GeV/c.

We are considering two options for the inner (downstream) detector. One possibility is a more complicated version of ORCID using 8 meters of N_2 as a radiator. An angular resolution of about 0.1 mr should be possible with such a device. This corresponds to a 3σ $\pi/K/p$ separation over the momentum range of 40-130 GeV/c. Figure 4.9 illustrates the capabilities of a 1 meter long Freon filled ORCID detector and an 8 meter, N_2 filled ORCID. The angular separation of the rings in units of σ are shown as a function of momentum for πK and Kp separation. The range over which $\pi/K/p$ separation is possible at the 3σ level can then be read from the curves.

The second option for the inner detector is again a Cerenkov ring imaging apparatus using multi-step avalanche chambers (MSAC) to detect the Cerenkov radiation. Recent work by Charpak and co-workers for E-605 at Fermilab has indicated that an 8 meter He radiator with a CaF_2 window viewed by a MSAC filled with Argon and Triethylamine (TEA) should be capable of $\pi/K/p$ separation in the momentum range of 85-300 GeV/c[24,25]. In figure 4.10, we compare the capabilities of a 1 meter Freon filled ORCID and an 8 meter He filled MSAC device. In the momentum range of 40-85 GeV/c $\pi/K/p$ would not be possible unless the particles passed through both detectors. An additional disadvantage of the 8 meter He radiator is that the average number of detected photoelectrons is about five. In contrast, the 8 meter N_2 ORCID should detect about 30 photoelectrons for each particle.

5.0 Cost and schedule estimates

The major costs for the experimentors are detailed in table 5. The total expenditure to construct the new equipment will be $1030K which will be spread over several fiscal years and shared by the experimenters at the various institutions. This cost should be compared with the $1105K value of existing equipment constructed during the two year preparation period for E-609. Though this figure of $1030K for new equipment may seem large at first inspection, it is completely consistent with the funding level granted to the collaborating institutions to construct E609.

Most of the new costs are associated with the construction of the downstream elements of the apparatus. The downstream calorimeter accounts for about $\frac{1}{2}$ of these new costs. This new downstream portion of the apparatus is extremely important for the study of jet photoproduction since the two high p_t jets tend to go forward in the cm frame. Another essential feature is the photon tagging system which will aid in the separation of three jet vs. four jet events. Its estimated cost of $35K seems to be a relatively small investment for the physics results it will enable.

Based on our experience in preparing the apparatus for E609, we estimate a construction period of about 2-3 years to build and test the new gear. This estimate depends on approval of the experiment and the availability of funds, of course, but should be relatively independent of research and development time. This is because most of the new equipment (hadron calorimeter and chambers) will essentially be duplications of what we've built for E609. The ORCID and the electromagnetic detector

which will require some R & D are presently in that stage. During the running of E609 these two devices should be tested and operated at least in prototype configuration.

This estimated construction period of 2-3 years is well matched to the estimated construction schedule for the Wide Band Beam. This schedule as given in reference 17 estimates that the Wide Band Beam would be completed $2\frac{1}{2}$ years after funds become available for construction. Should these funds become available in FY 82 as part of the Tevatron II project, the beam line could be completed as early as mid-year 1984. Consequently, we are requesting approval of this experiment as soon as possible in order to obtain the funding necessary to complete the construction of the new equipment at the same time that the Wide Band Beam is completed.

Finally, we request 1500 hours of beam time. This request includes 500 hours for tune-up, calibration, and some hadron beam running. The remaining 1000 hours will be for data runs with the photon beam.

REFERENCES

1. H. Fritzsch and P. Minkowski, Physics Letters 69B, 316, (1977).
2. D. W. Duke and J. F. Owens, Physical Review D22, 2280 (1980).
3. J. F. Owens, Physical Review D21, 54 (1980).
4. M. Corcoran, Monte Carlo Jets, E-609 Internal Note, unpublished.
5. S. D. Ellis and M. B. Kislinger, Physical Review D8, 4098 (1973).
6. B. L. Combridge, J. Kripfganz, and J. Ranft, Physics Letters 70B, 234 (1977).
7. R. D. Field, CALT-68-688, (1978); R.D. Field, Physical Review Letters 40, 991 (1978); R.P. Feynman, R.D. Field, and G.C. Fox, Physical Review D18, 3320 (1978).
8. J. F. Owens and J. D. Kimel, Physical Review D18, 3313 (1978).
9. R. J. Dewitt, et al., Physical Review D19, 2046 (1979).
10. W. Selove et al., Results from a Two-Arm Calorimeter-Array Jet Experiment, International Conference on High Energy Physics, P. 165, Tokyo (1978).
11. A. R. Erwin et al., A Preliminary Look at Hadron Structure with a Double Arm Calorimeter, AIP Conference Proceedings No. 45 (Vanderbilt Conference, 1978).
12. M. Corcoran et al., Physical Review Letters 44, 514 (1980).
13. M. Corcoran et al., Physical Review D21, 641 (1980).
14. M. Dris et al., Physical Review D19, 1361 (1979).
15. See for example H. Anderson, H. S. Matis, and L. C. Myrianthopoulos, Physical Review Letters 40, 1061 (1978).
16. L. Cormell and J. F. Owens, Physical Review D22, 1609 (1980).

17. J. Butler et al., Design for a New Wide Band Neutral Beam for the Tevatron, Fermilab TM-963 (1980).

18. G. Luste, Jet Photoproduction at the Tevatron, in the Proceedings of the Tevatron Workshop, G.L. Kane, editor, Fermilab, July, 1980, (to be published.)

19. T. Fields, et al., Jet Production in 1000 GeV Hadron Collisions, submitted to PAC, Fermilab, February, 1981.

20. W. Selove, et al., Some Energy Resolution Effects for Hadron Jets in a Calorimeter Array, University of Pennsylvania Report UPR-75E, 1980 (to be published in Physica Scripta).

21. M. Dris, Nuclear Instruments and Methods 158, 89 (1979).

22. B. Yost, et al., IEEE Transactions on Nuclear Science 26, 105 (1979).

23. B. Robinson, A New Type of Cherenkov Imaging Detector, University of Pennsylvania Report UPR-76E, 1980 (to be published in Physica Scripta).

24. A. Breskin et al., Advances in Vacuum Ultraviolet Detection with Multistep Gaseous Detectors and Application to Cerenkov Ring Imaging, CERN-EP/80-220, December, 1900.

25. J.R. Hubbard et al., Nuclear Instuments and Methods 176, 233 (1980).

Table 1 Photon Flux

Photon rates per 10^{12} protons on target

Ee	Eγ (±10%)	Rate /10^{12}p
600 GeV	450 GeV	6.5×10^{5}
600	550	5.0×10^{5}
450	200	9.3×10^{6}
450	300	5.8×10^{6}
450	400	3.9×10^{6}

Table 2 Photon Beams[17, 18]

	PRESENT			FUTURE	
	FNAL Tagged Photon	FNAL Broad Bond	CERN Ω Beam	Tevatron Tagged Photon	Tevatron Wide Band Beam
Primary protons	400 GeV/c	400 GeV/c	210 GeV/c	1 TeV	1 TeV
	6×10^{12}	1×10^{12}	1×10^{13}	3×10^{12}	1×10^{12}
Eγ (GeV)	30-150	50-250	20-70	150-300	200-500
Nγ	5×10^{6}	$\sim10^{7}$	2×10^{5}	$\sim10^{7}$	$\sim2\times10^{7}$
$\mu/m^2/10^{12}p$	$\sim10^{4}$	$\sim2\times10^{5}$	?	?	$<8\times10^{5}$
hadrons/γ	$<10^{-6}$	~Few %	?	?	$\sim1\times10^{-5}$

Table 3 Calculated Event Rates

$\gamma p \rightarrow$ jet + x at 90^{o}cm

Ee(GeV)	Eγ(GeV)	P_T(GeV/c)	$E\frac{d^3\sigma}{dp^3}$	N_{evts} (100 hrs.)
450	200	3	2.2×10^{-32}	7100
		4	3.3×10^{-33}	1400
		5	6.7×10^{-34}	360
		6	1.7×10^{-34}	110
		7	3.8×10^{-35}	29
		8	6.8×10^{-36}	6
450	400	3	4.1×10^{-32}	5400
		4	6.8×10^{-33}	1200
		5	1.4×10^{-33}	310
		6	4.6×10^{-34}	122
		7	1.5×10^{-34}	45
		8	4.7×10^{-35}	17
		9	1.8×10^{-35}	7
		10	6.3×10^{-36}	3
600	500	3	5.0×10^{-32}	1000
		4	9.7×10^{-33}	258
		5	2.3×10^{-33}	78
		6	6.4×10^{-34}	26
		7	2.2×10^{-34}	10
		8	8.6×10^{-35}	5
		9	3.4×10^{-35}	2

Table 4 Tagging System: Electron Shower Detectors

The shower detectors are Pb/scintillator sandwiches 10cm x 10cm x 24 X_o. The rates and E_e are given for a 600 GeV/c beam.

Detector No.	Z from Pb radiator (meters)	$\bar{X}$ from beam line (cm)	$\bar{E}_e$ (GeV)	$\frac{\Delta E_e}{E_e}$ (%)	Rate/10^{12}
1	10	25	240	1.4	8.6×10^{5}
2	"	35	170	1.7	3.5×10^{5}
3	"	45	130	1.9	1.9×10^{5}
4	"	55	110	2.1	1.2×10^{5}
5	"	65	92	2.3	8.0×10^{4}
6	"	75	80	2.5	5.8×10^{4}
7	"	85	71	2.6	4.4×10^{4}
8	"	95	63	2.8	3.4×10^{4}
9	20	55	55	3.0	5.0×10^{4}
10	"	65	46	3.2	3.5×10^{4}
11	"	75	40	3.5	2.6×10^{4}
12	"	85	35	3.7	2.0×10^{4}
13	"	95	32	3.9	1.6×10^{4}
14	"	105	29	4.1	1.3×10^{4}
15	"	115	26	4.3	1.1×10^{4}
16	"	125	24	4.5	8.9×10^{3}

Table 5 Cost Estimates for the Apparatus in 1980 $

	Element	Existing Value ($)	New Cost ($)
1.	Upstream hadron calorimeter	700 K	
2.	Downstream hadron calorimeter	15 K	480 K
3.	Upstream electromagnetic detector		100 K
4.	Downstream electromagnetic detector		65 K
5.	Upstream drift chambers and PWC's	190 K	
6.	Downstream drift chambers and PWC's		100 K
7.	Upstream $\bar{\nu}$ Cerenkov detector	40 K	
8.	Downstream $\bar{\nu}$ Cerenkov detector		
	ORCID		80 K
	(MSAC)		(70 K)
	(segmented threshold)		(60 K)
9.	Electron tagging system		
	electron shower detectors		20 K
	drift chambers		15 K
10.	Muon anti-counters	5 K	5 K
11.	"Super modules" for housing calorimeter	35 K	35 K
12.	Special electronics cables, and miscellaneous items	120 K	130 K
	Total	1105 K	1030 K

Figure Captions

1.1: Typical high P_t interactions in the CM frame.

(a) Photoproduced three jet event at $p_t = 4$, $\sqrt{s} = 19.4$ GeV

(b) Photoproduced three jet event at $p_t = 4$, $\sqrt{s} = 30.6$. GeV

(c) Hadron produced jet event at $p_t = 4$, $\sqrt{s} = 19.4$. GeV

(d) Hadron produced jet event at $p_t = 8$, $\sqrt{s} = 30.6$. GeV.

2.1: Feynman diagrams for the contributions to high p_t jet photoproduction.

(a) Point-like coupling of the photon in the QCD Compton and fusion diagrams giving rise to three jet events (the crossed diagrams are not shown).

(b) Hadron-like coupling of the photon giving rise to four jet events.

(c) Vector meson coupling of the photon giving rise to four jet events.

2.2: Prediction for the experimental resolution in three vs. four jet events. The QCD prediction for the two processes has been smeared by the experimental resolution for the jets. The "data" points plotted indicate the statistical accuracy expected for a 100 hr. run.

2.3: Photon structure function as calculated in reference 2 in the QCD leading log approximation and in the VMD approximation.

2.4: Cross-section for $\gamma p \rightarrow$ jet + x as calculated in reference 3. The contributions from the three jet and four jet processes are shown.

2.5: Comparison of photoproduced cross-section versus the hadron produced cross-section at high p_t. The contributions from QCD and VMD are shown separately. The sensitivity that can be achieved at the level of 1 event/hour is also shown.

2.6: Photoproduced jet cross-sections at $\theta^* = 90^\circ$ for $\sqrt{s}$ = 19.4, 27.4, and 30.6 GeV.

2.7: Predictions for the angular dependence of R_g as defined in the text at $\sqrt{s}$ = 19.4 from all of the QCD contributions.

3.1: Optical elements and their relative positioning in the Wide Band Beam.

3.2: Wide Band Beam pion flux for $\pm$ 15% momentum acceptance.

3.3: Wide Band Beam electron flux for a $\pm$ 15% momentum acceptance.

3.4: Wide Band Beam bremsstrahlung photon flux as produced by electron beams of 450 and 600 GeV/c momentum radiating from a 30% X_o target.

3.5: Schematic drawing of the upstream end of the tagging system. The momentum of the electrons is measured by the "spectrometer" consisting of the final bend string B3 and the drift chambers. The position of the electrons at the radiator is determined by the scintillation hodoscope.

3.6: Schematic drawing for the downstream end of the tagging system. the momentum of the recoiling electrons is determined by the Pb/scintillator shower detectors. The direction of the radiated photon is determined from the 1 mm hodoscope and the event vertex in the experimental target (not shown). The anti-counters around the beam aid in rejecting hadronic interactions, tridents, and other interactions in the radiator.

4.1: Plan view of apparatus. The apparatus consists of a large acceptance magnetic spectrometer, two electron and hadron calorimeters, and two imaging Cerenkov detectors. All of these detectors are discussed individually in the text.

4.2: Plan view of the apparatus indicating the center of mass polar angle coverage at $\sqrt{s}$ = 19.4 GeV (beam left) and $\sqrt{s}$ = 30.6 GeV (beam right).

4.3: Front face of upstream calorimeter illustrating the "fly's eye" segmentation of the modules.

4.4: Front face of the downstream calorimeter.

4.5: Details of the optical system of the calorimeter modules. Light produced in the scintillator is absorbed and re-radiated by the BBQ wavelength shifter. This light is then piped via total internal reflection to the phototube.

4.6: Schematic drawing of the prototype electron/photon detector. It consists of a Pb/scintillator sandwich with BBQ "readout". The position of the showers is determined by cathode strip PWC's.

4.7: Schematic drawing of typical calorimeter trigger. The Σp_t measured in the modules in the lined regions forms the trigger. This trigger is designed to select two high p_t jets centered at about 90^o and 40^o, respectively in the center of mass.

4.8: Schematic drawing of ½ of ORCID. Cerenkov light produced in the Freon 12 radiator is focussed by two spherical mirrors onto an image intensifier. This light is converted by a high resolution CCD. The ring pattern of the "struck" photosites in the CCD are used to determine the Cerenkov angle.

4.9: Comparison of a 1 m Freon-filled ORCID and an 8 meter N_2-filled detector. The ORCID would provide π/K/p separation in the momentum range from 14-40 GeV/c while the N_2 device would provide separation in the range from 40-130 GeV/c.

4.10: Comparison a 1 m Freon-filled ORCID and an 8 m He-filled detector. The He detector would provide π/K/p separation in the momentum range from 86 - 300 GeV/c.

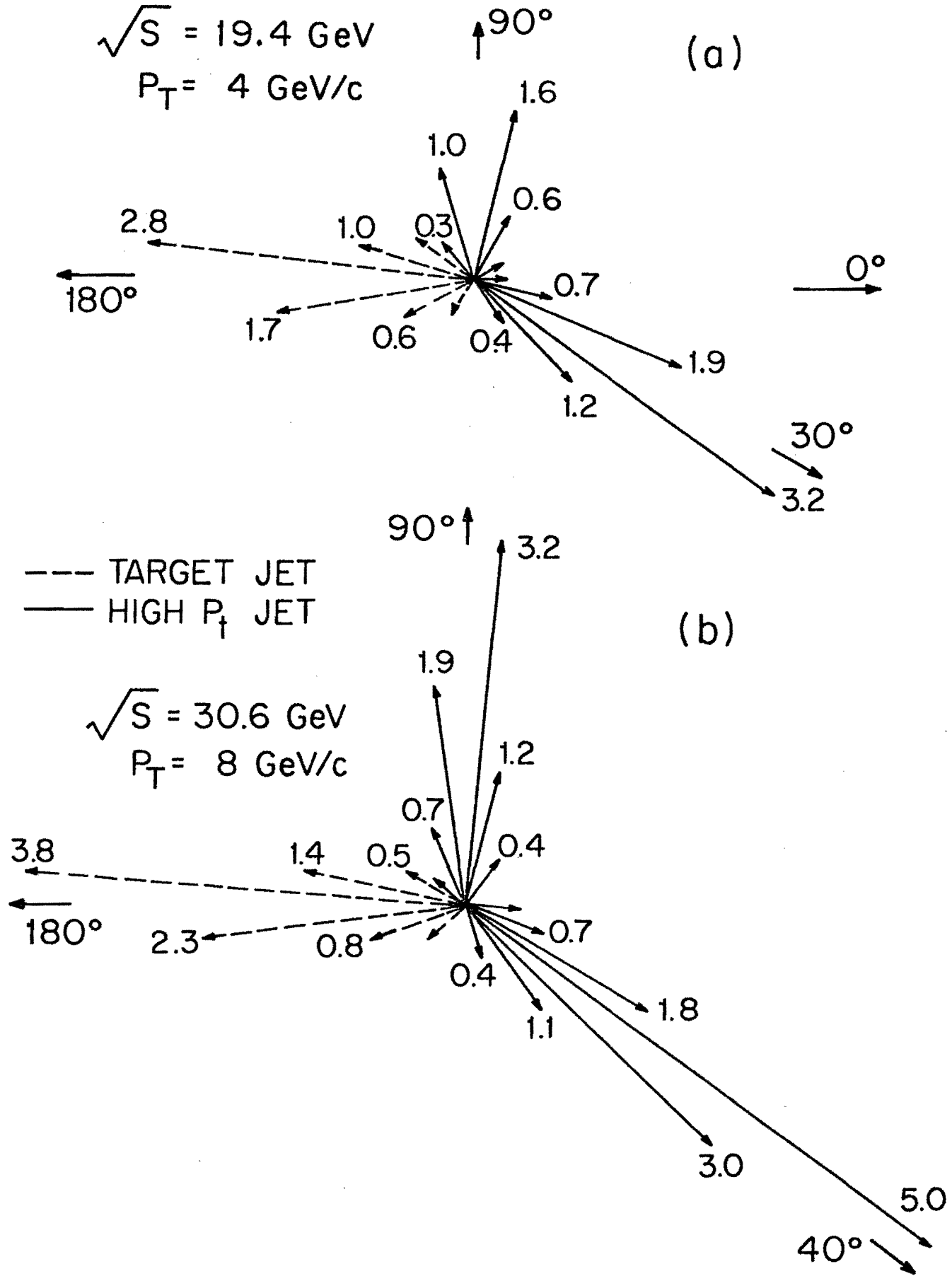
√S = 19.4 GeV
P_T = 4 GeV/c
90°
(a)
1.6
1.0
0.6
2.8
1.0
0.3
0°
180°
0.7
1.7
0.6
0.4
1.9
1.2
30°
3.2
90°
3.2
--- TARGET JET
—— HIGH P_t JET
(b)
1.9
√S = 30.6 GeV
P_T = 8 GeV/c
1.2
0.7
3.8
1.4
0.5
0.4
180°
2.3
0.8
0.7
0.4
1.8
1.1
3.0
5.0
40°

Figure 1.1

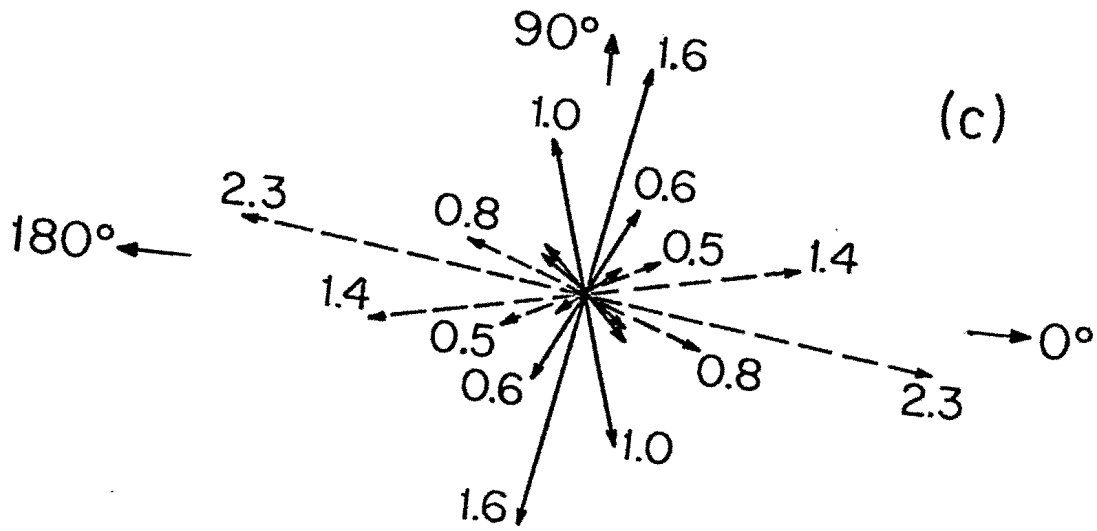
90°
1.6
1.0
(c)
2.3
0.8
0.6
180°
0.5
1.4
1.4
0.5
0°
0.8
0.6
2.3
1.0
1.6

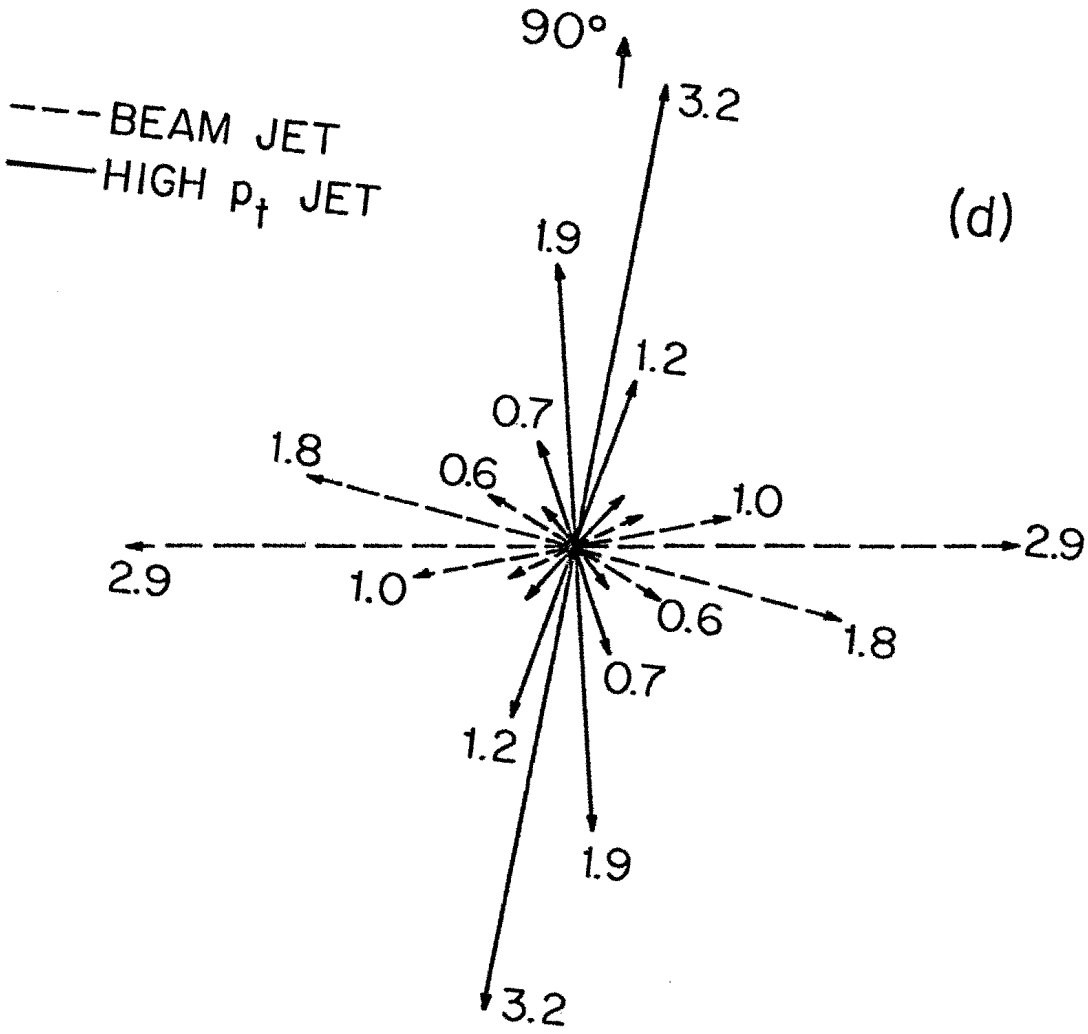
90°
3.2
---BEAM JET
——HIGH p_t JET
(d)
1.9
1.2
0.7
1.8
0.6
1.0
2.9
2.9
1.0
0.6
1.8
0.7
1.2
1.9
3.2

Figure 1.1

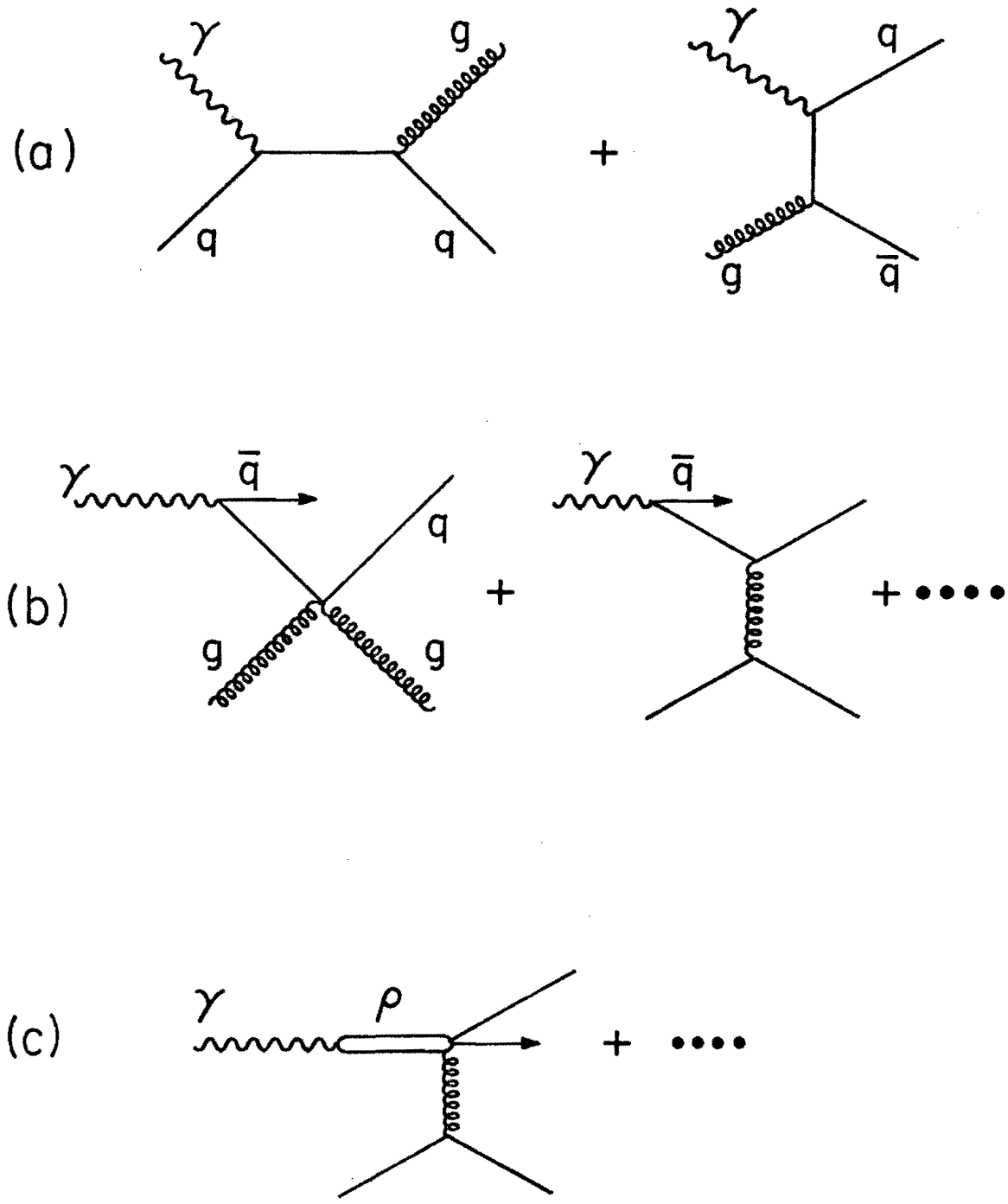

Figure 2.1

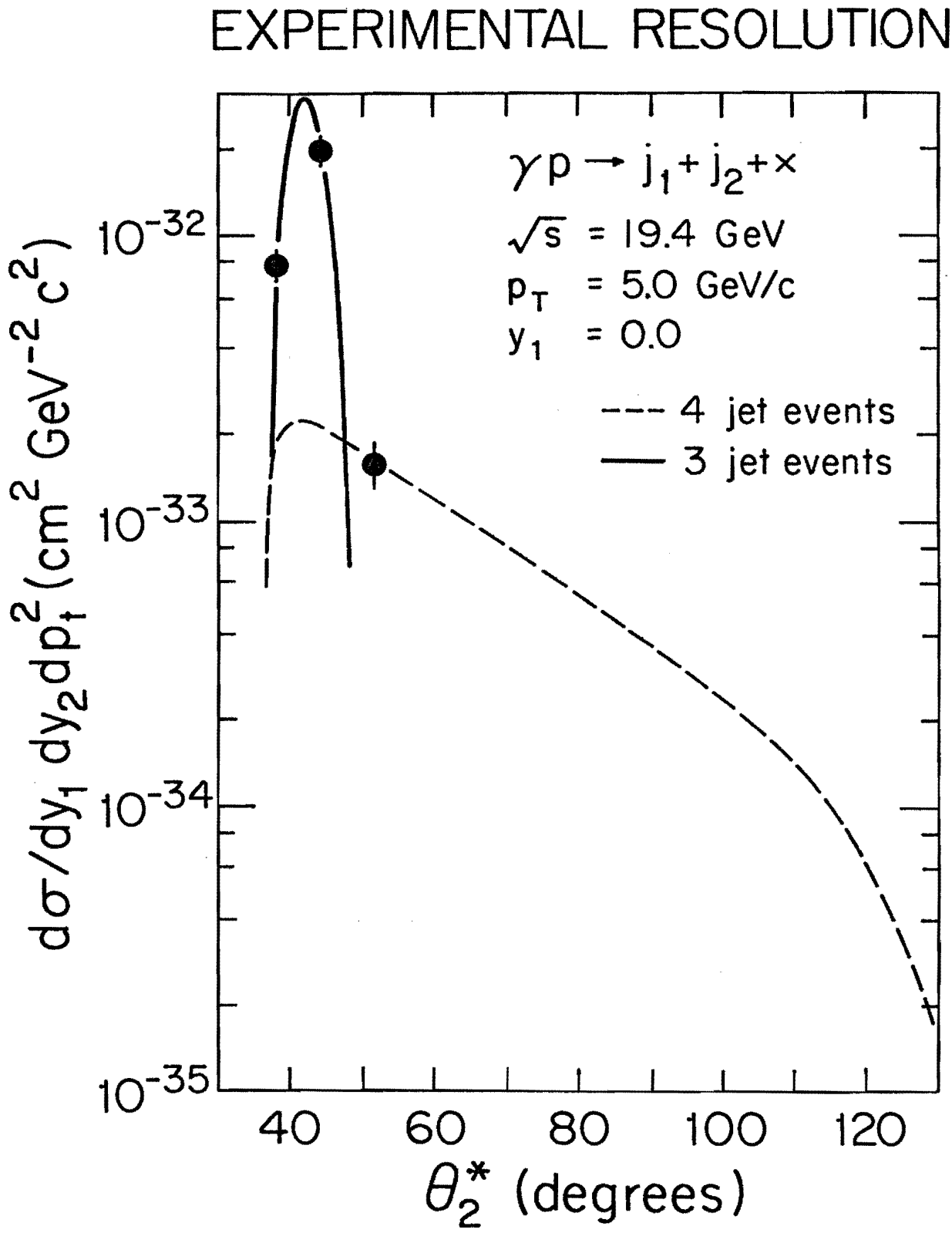
EXPERIMENTAL RESOLUTION
$\gamma p \rightarrow j_1 + j_2 + X$
$\sqrt{s}$ = 19.4 GeV
p_T = 5.0 GeV/c
y_1 = 0.0
--- 4 jet events
— 3 jet events
$d\sigma/dy_1\, dy_2 dp_t^2$ (cm^2 GeV^{-2} c^2)
10^{-32}
10^{-33}
10^{-34}
10^{-35}
40
60
80
100
120
θ_2^* (degrees)

Figure 2.2

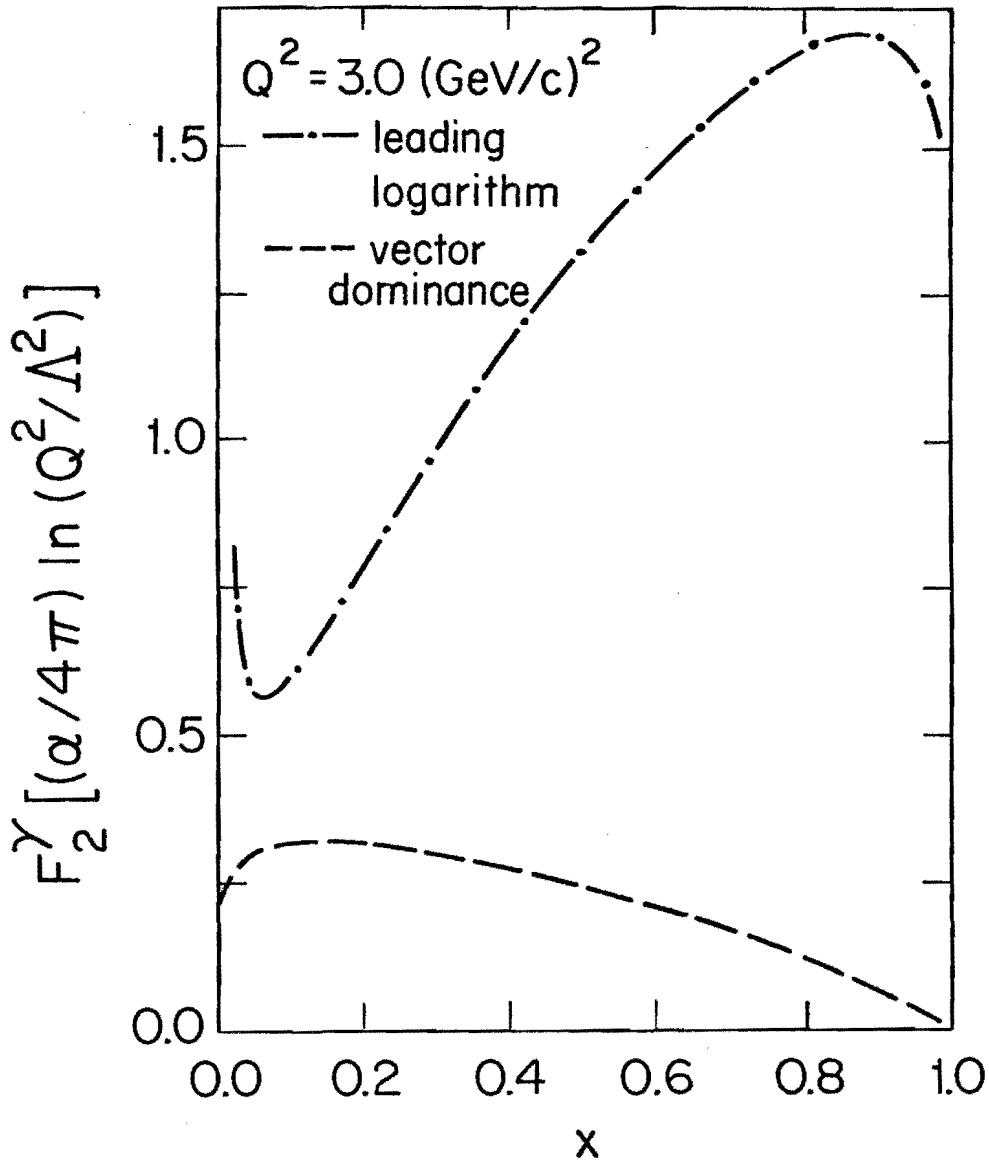
$Q^2 = 3.0$ (GeV/c)^2
leading logarithm
vector dominance
$F_2^\gamma [(\alpha/4\pi) \ln (Q^2/\Lambda^2)]$
1.5
1.0
0.5
0.0
0.0
0.2
0.4
0.6
0.8
1.0
x

Figure 2.3

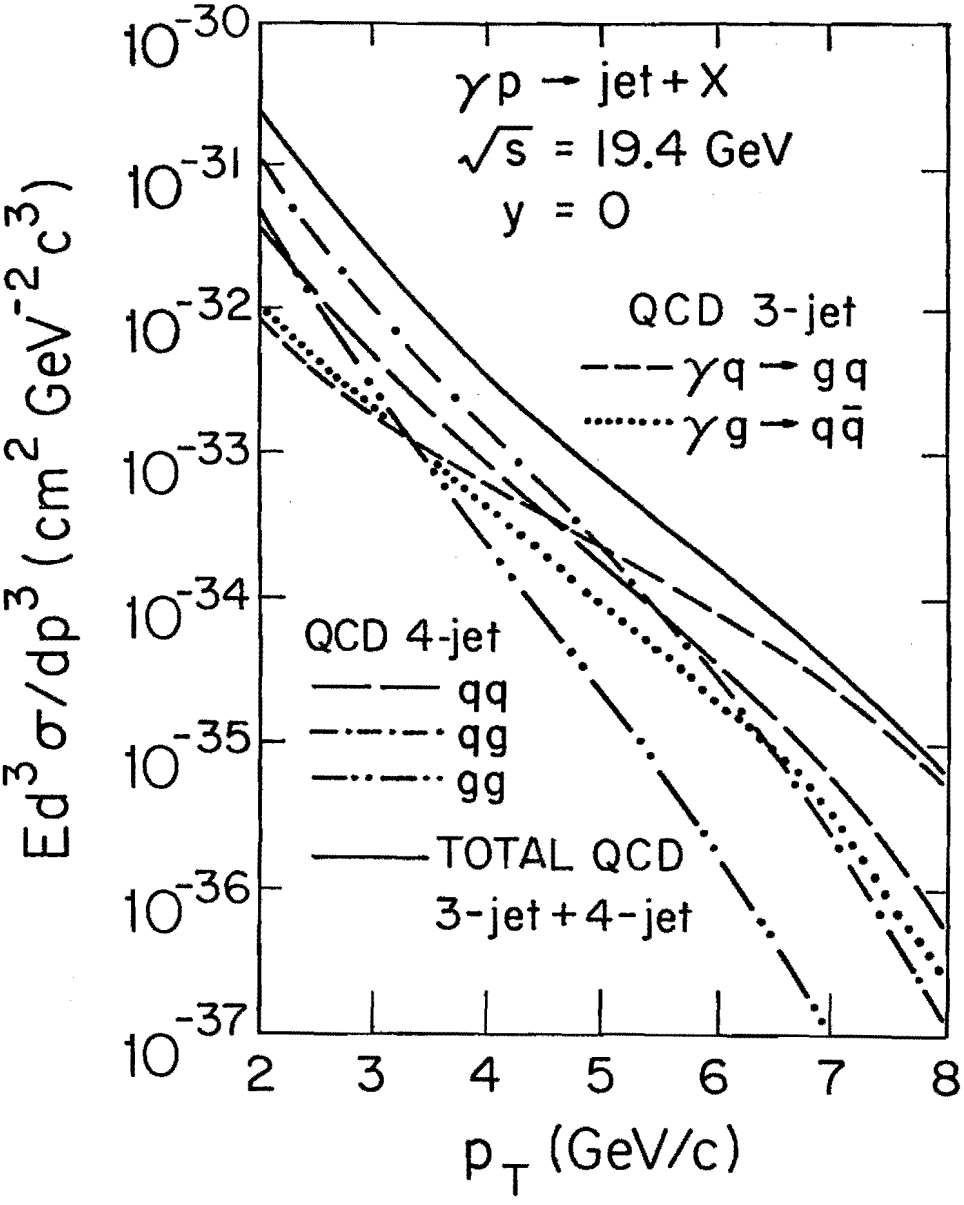
$\gamma p \rightarrow$ jet + X
$\sqrt{s}$ = 19.4 GeV
y = 0
QCD 3-jet
$\gamma q \rightarrow gq$
$\gamma g \rightarrow q\bar{q}$
QCD 4-jet
qq
qg
gg
TOTAL QCD
3-jet + 4-jet
$Ed^3\sigma/dp^3$ (cm^2 GeV^{-2}c^3)
p_T (GeV/c)
10^{-30}
10^{-31}
10^{-32}
10^{-33}
10^{-34}
10^{-35}
10^{-36}
10^{-37}
2
3
4
5
6
7
8

Figure 2.4

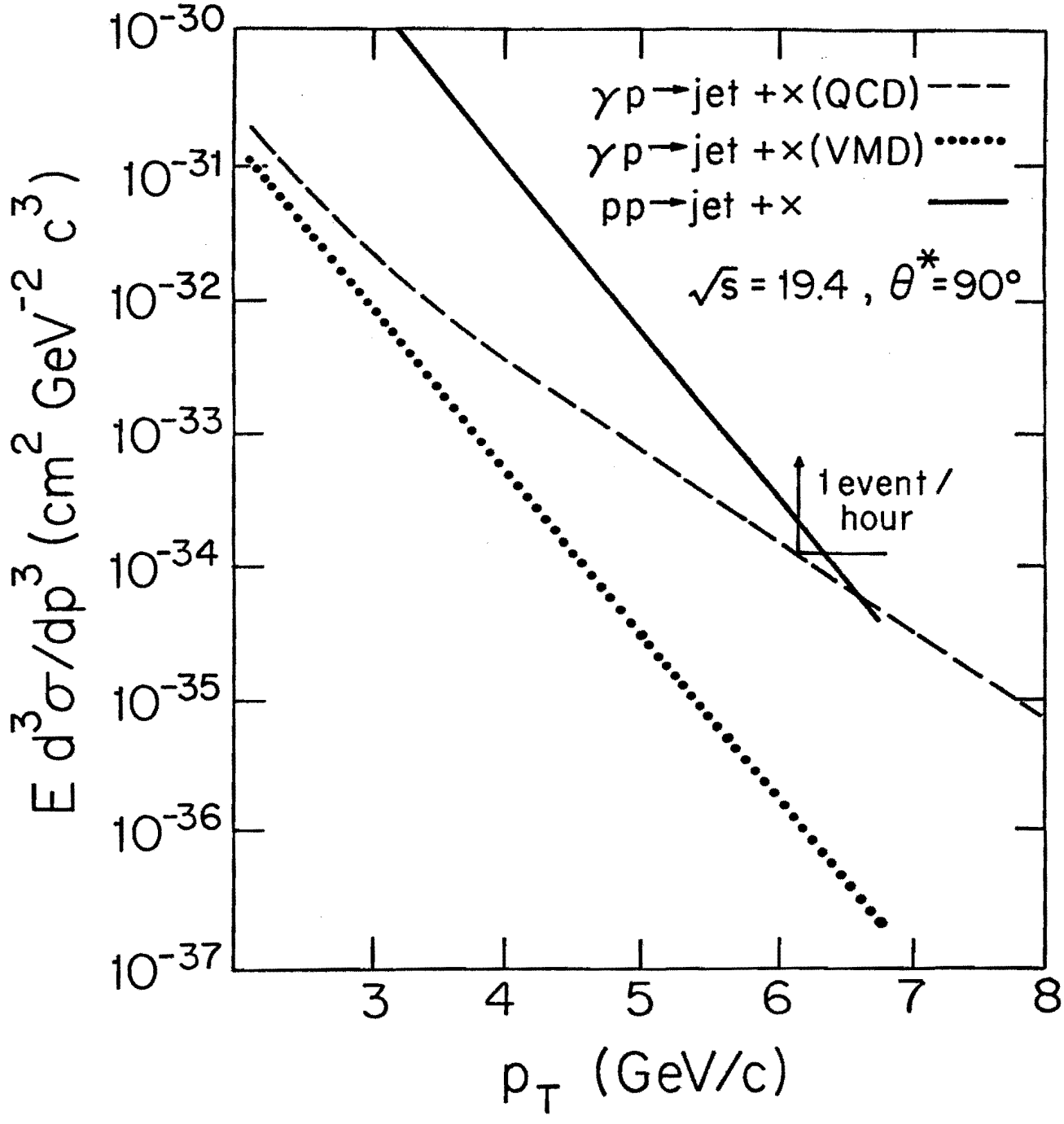
10^{-30}
10^{-31}
10^{-32}
10^{-33}
10^{-34}
10^{-35}
10^{-36}
10^{-37}
$E\,d^3\sigma/dp^3\ (cm^2\ GeV^{-2}\ c^3)$
3
4
5
6
7
8
p_T (GeV/c)
$\gamma p \rightarrow$ jet $+\times$ (QCD)
$\gamma p \rightarrow$ jet $+\times$ (VMD)
$pp \rightarrow$ jet $+\times$
$\sqrt{s} = 19.4$, $\theta^* = 90°$
1 event / hour

Figure 2.5

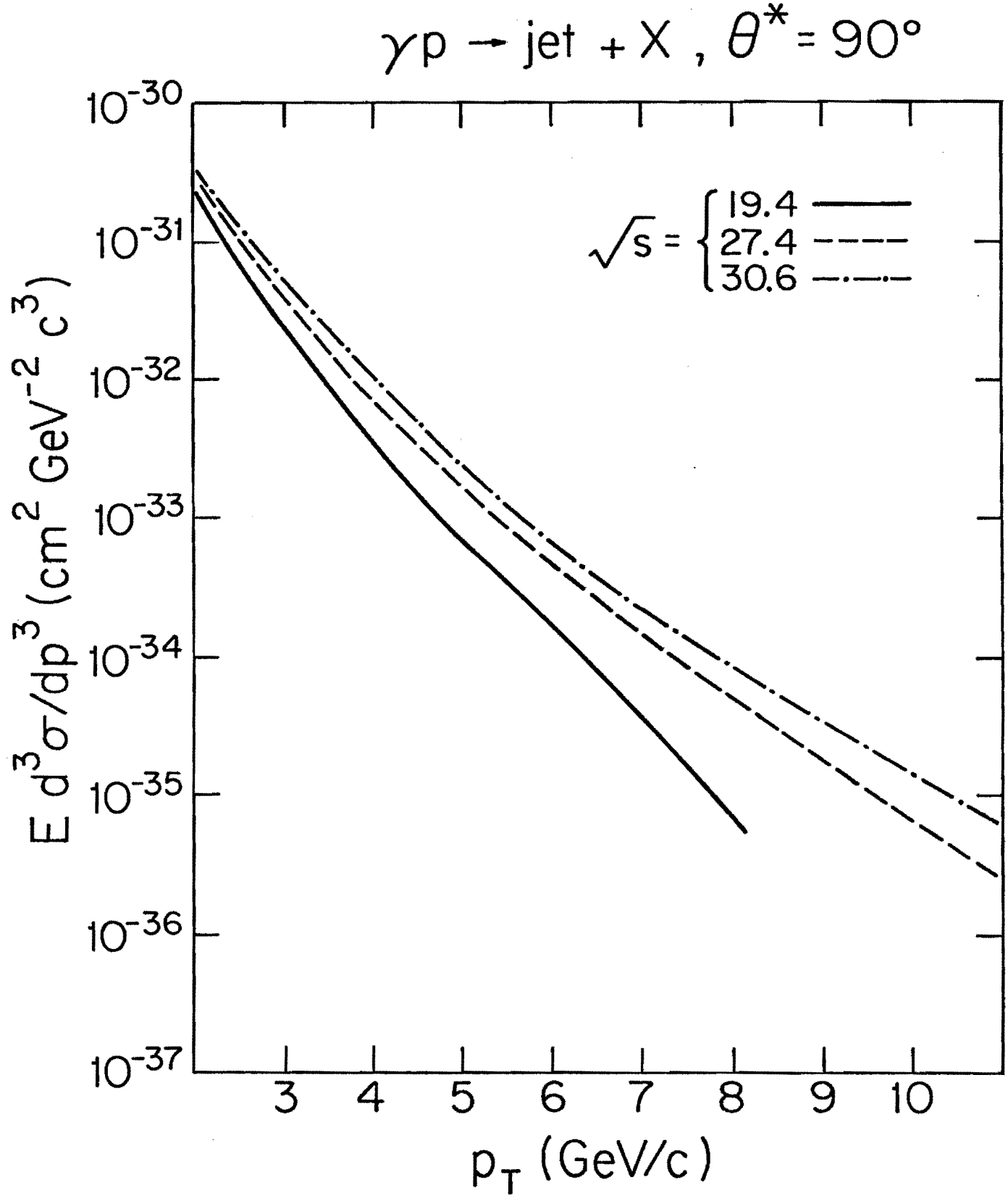
γp → jet + X , θ* = 90°
√s = 19.4
27.4
30.6
E d³σ/dp³ (cm² GeV⁻² c³)
10⁻³⁰
10⁻³¹
10⁻³²
10⁻³³
10⁻³⁴
10⁻³⁵
10⁻³⁶
10⁻³⁷
3
4
5
6
7
8
9
10
p_T (GeV/c)

Figure 2.6

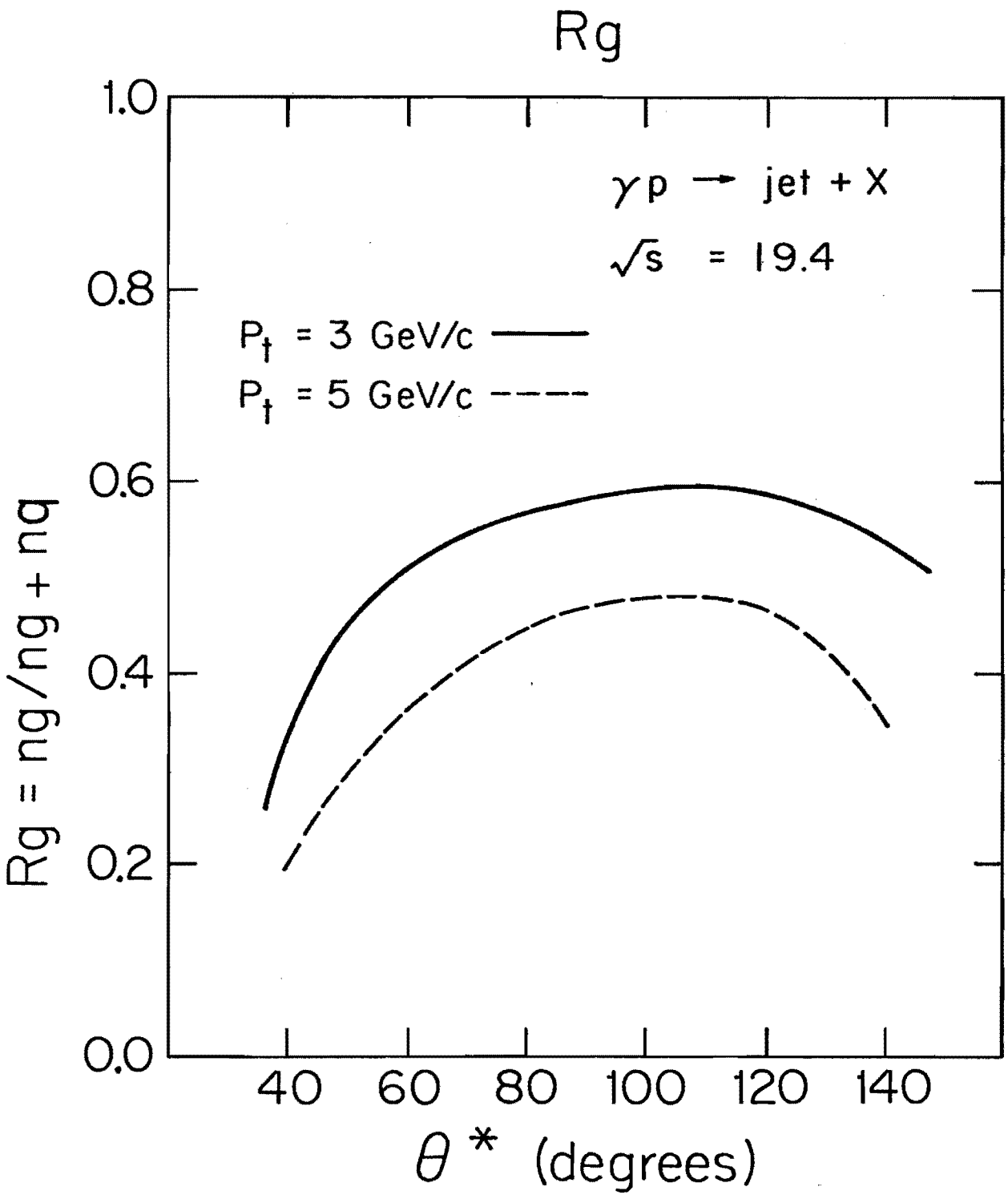
Rg
1.0
0.8
0.6
0.4
0.2
0.0
γp → jet + X
√s = 19.4
P_t = 3 GeV/c
P_t = 5 GeV/c
Rg = ng/ng + nq
40
60
80
100
120
140
θ * (degrees)

Figure 2.7

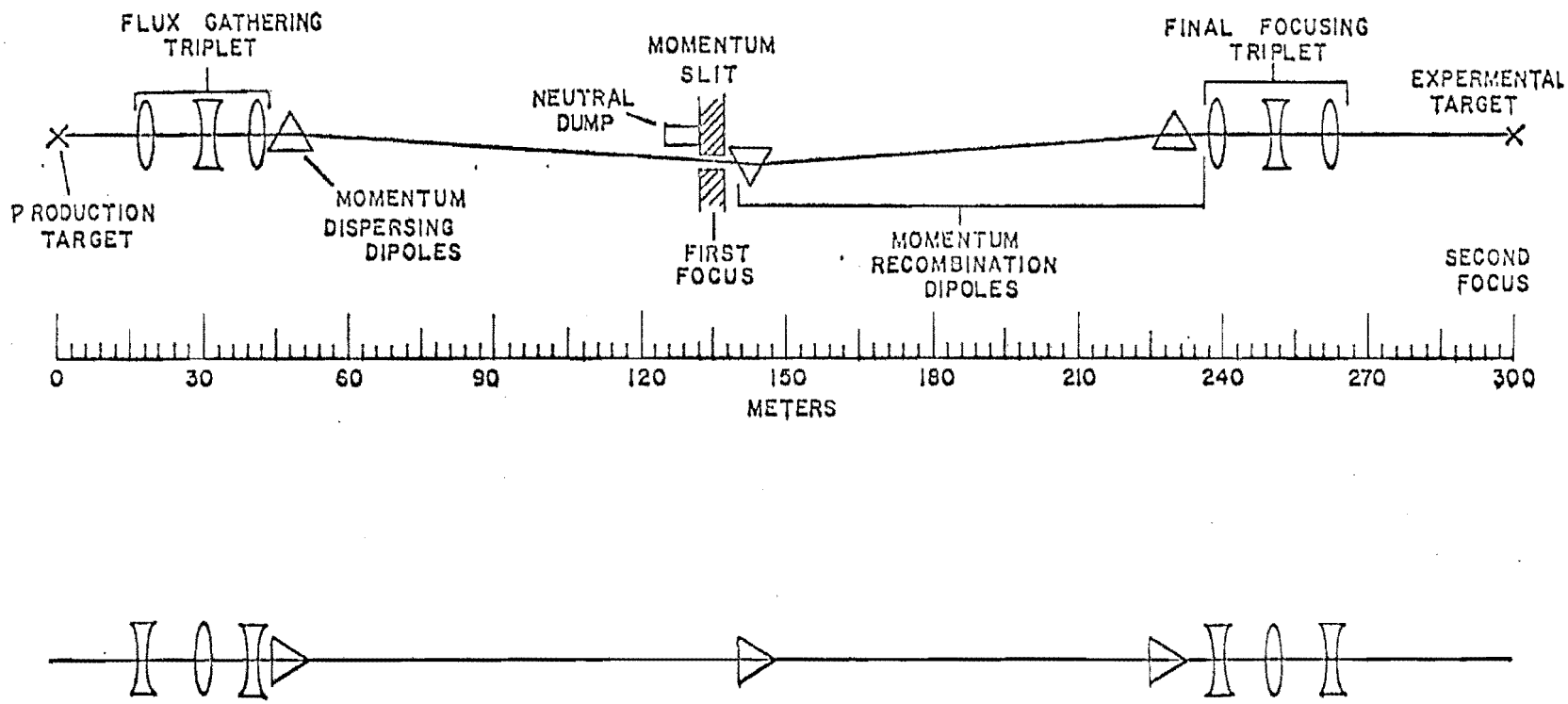
FLUX GATHERING TRIPLET
MOMENTUM SLIT
NEUTRAL DUMP
FINAL FOCUSING TRIPLET
EXPERMENTAL TARGET
P RODUCTION TARGET
MOMENTUM DISPERSING DIPOLES
FIRST FOCUS
MOMENTUM RECOMBINATION DIPOLES
SECOND FOCUS
0
30
60
90
120
150
180
210
240
270
300
METERS

Figure 3.1

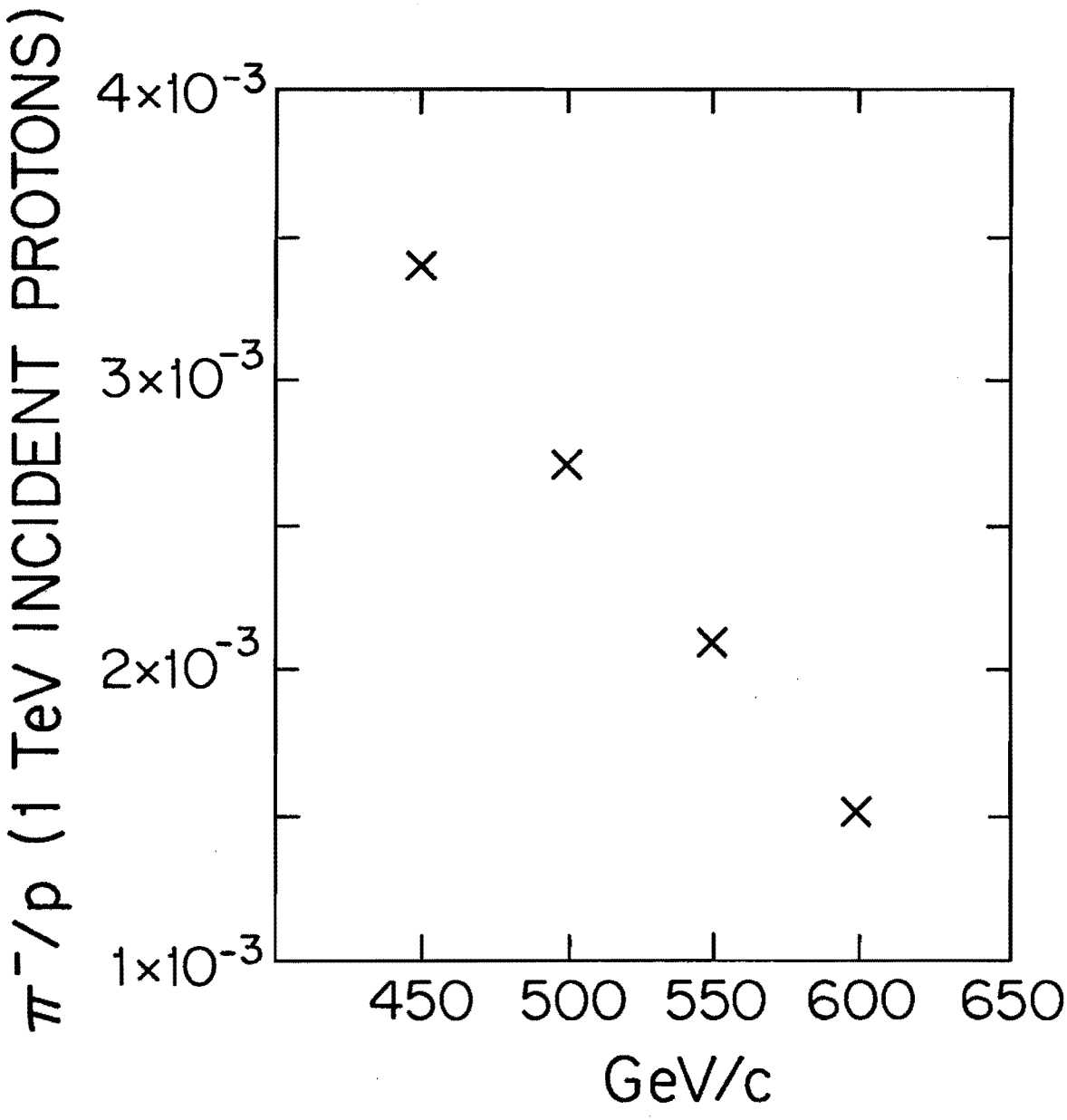
π^-/p (1 TeV INCIDENT PROTONS)
4×10^{-3}
3×10^{-3}
2×10^{-3}
1×10^{-3}
450
500
550
600
650
GeV/c

Figure 3.2

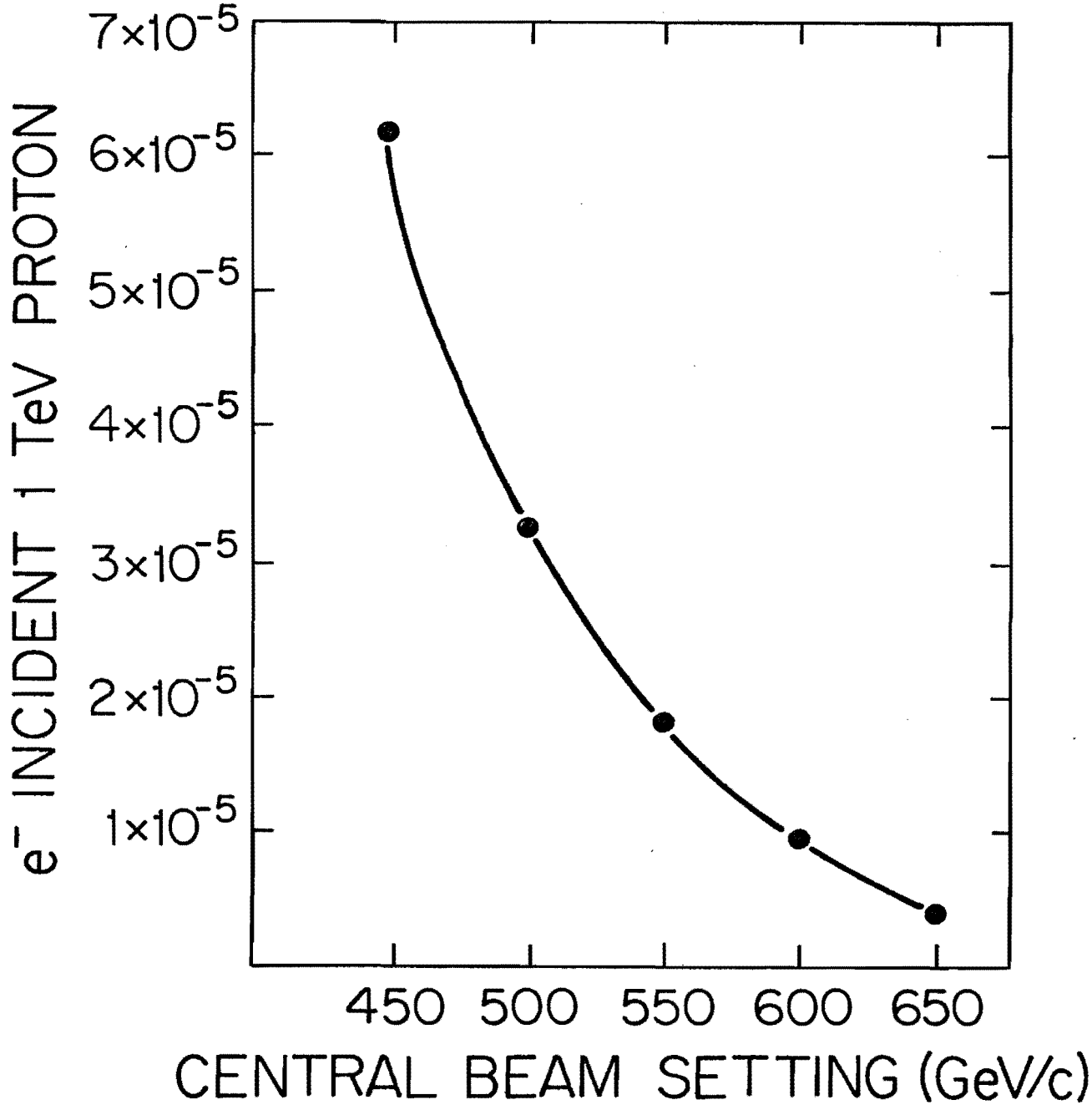
7×10⁻⁵
6×10⁻⁵
5×10⁻⁵
4×10⁻⁵
3×10⁻⁵
2×10⁻⁵
1×10⁻⁵
e⁻ INCIDENT 1 TeV PROTON
450 500 550 600 650
CENTRAL BEAM SETTING (GeV/c)

Figure 3.3

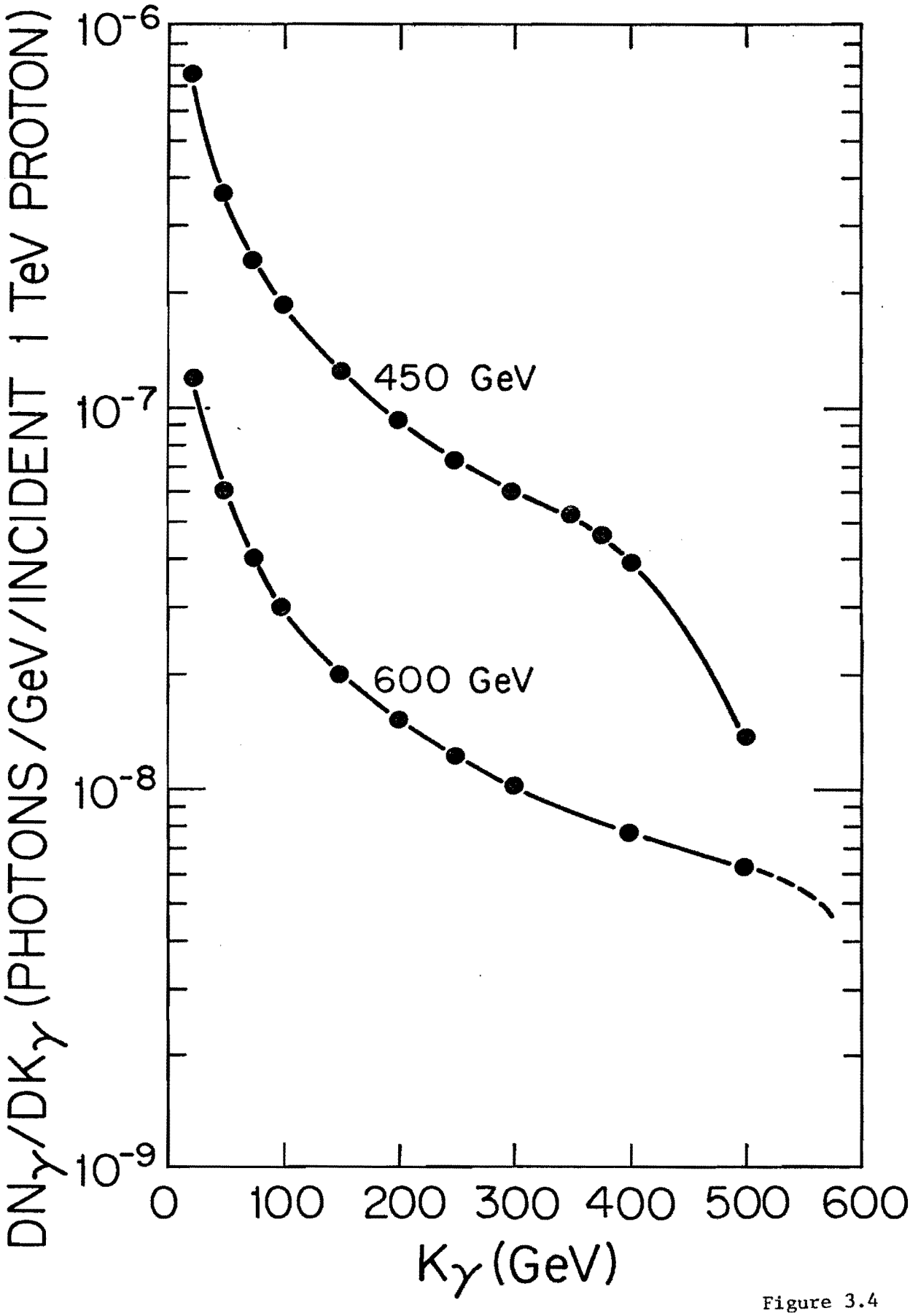
DN_γ/DK_γ (PHOTONS/GeV/INCIDENT 1 TeV PROTON)
10^{-6}
10^{-7}
10^{-8}
10^{-9}
450 GeV
600 GeV
0
100
200
300
400
500
600
K_γ (GeV)

Figure 3.4

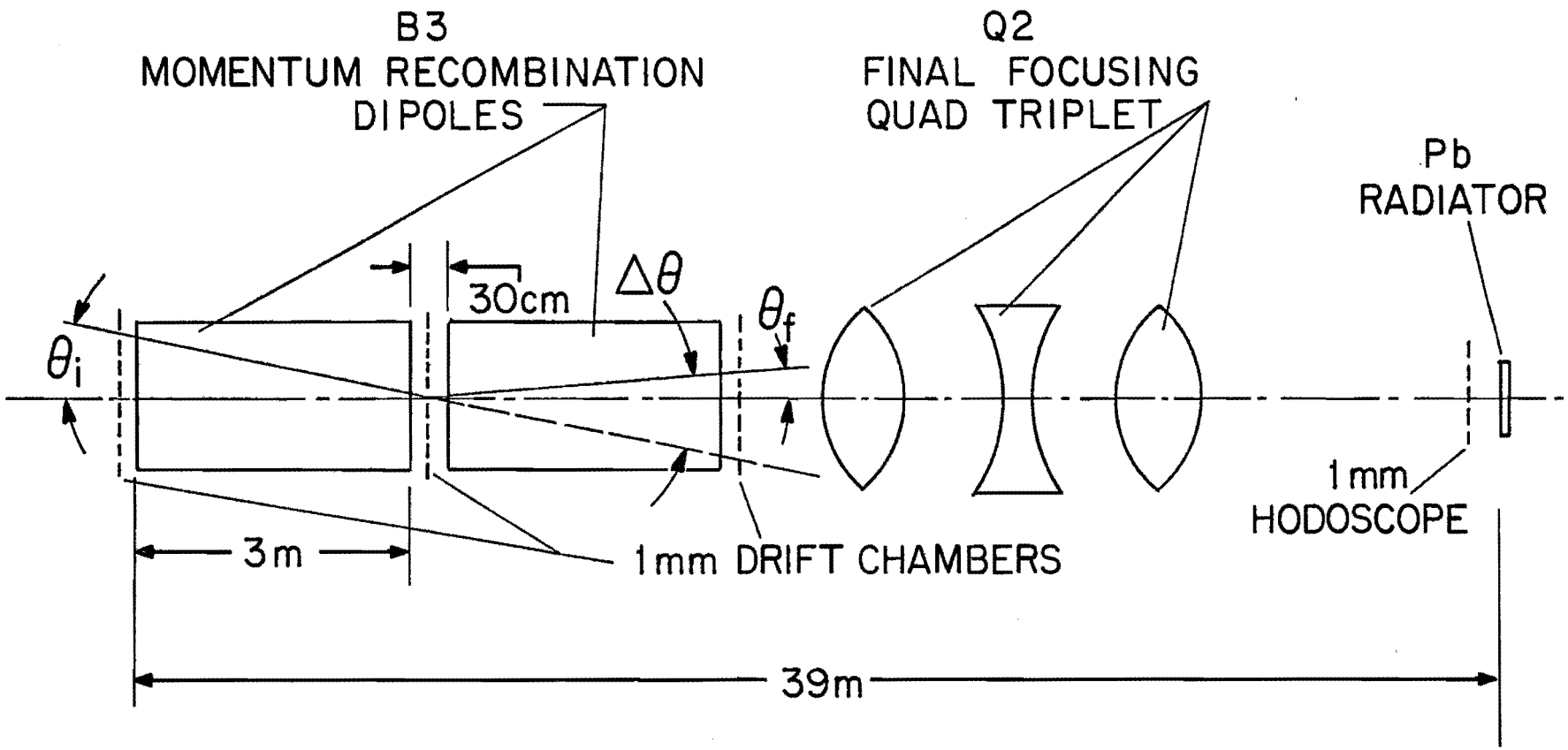
B3
MOMENTUM RECOMBINATION
DIPOLES
Q2
FINAL FOCUSING
QUAD TRIPLET
Pb
RADIATOR
30cm
Δθ
θf
θi
3m
1mm DRIFT CHAMBERS
1mm
HODOSCOPE
39m

Figure 3.5

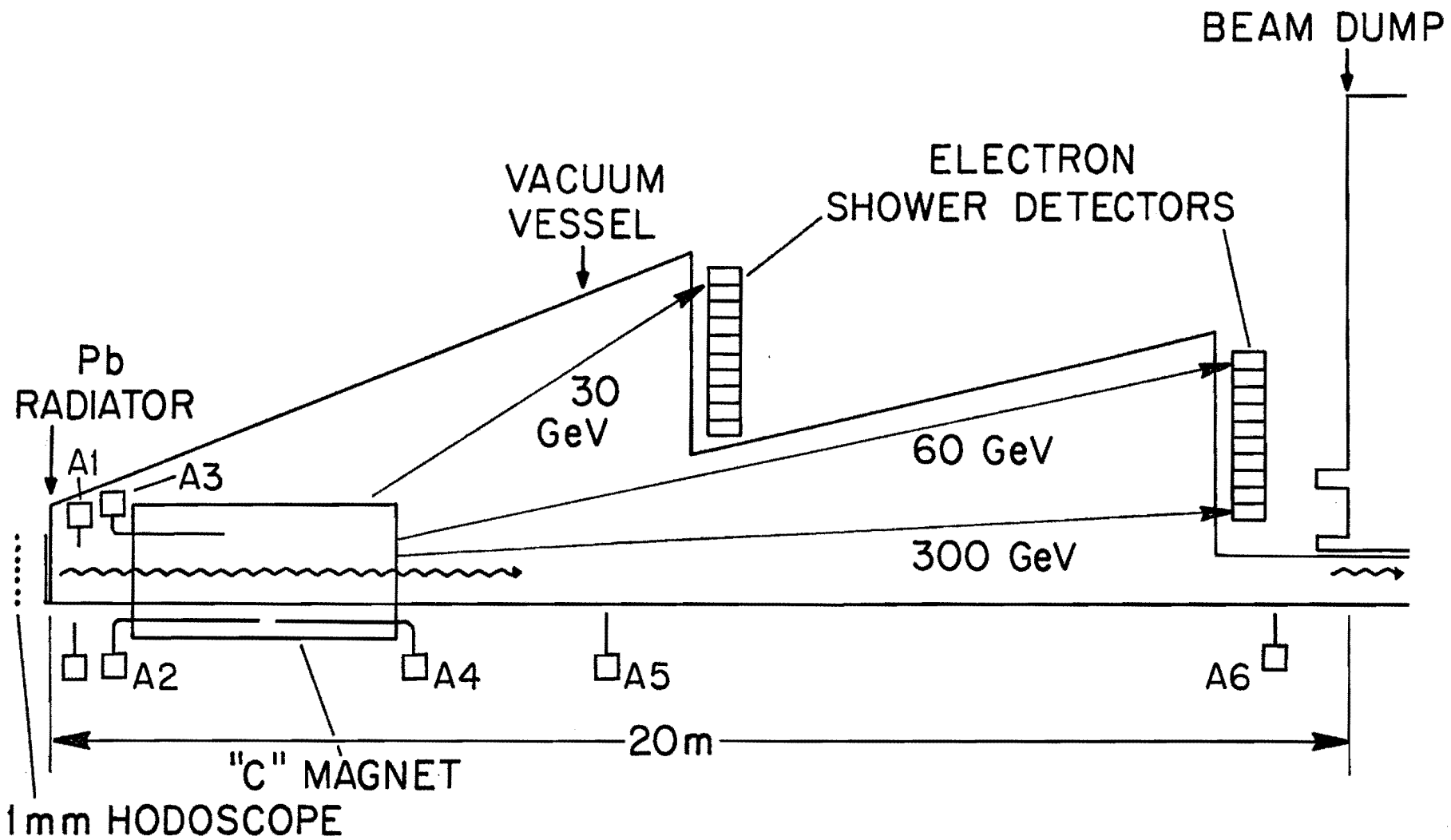
BEAM DUMP
VACUUM
VESSEL
ELECTRON
SHOWER DETECTORS
Pb
RADIATOR
A1
A3
30
GeV
60 GeV
300 GeV
A2
A4
A5
A6
20m
"C" MAGNET
1mm HODOSCOPE

Figure 3.6

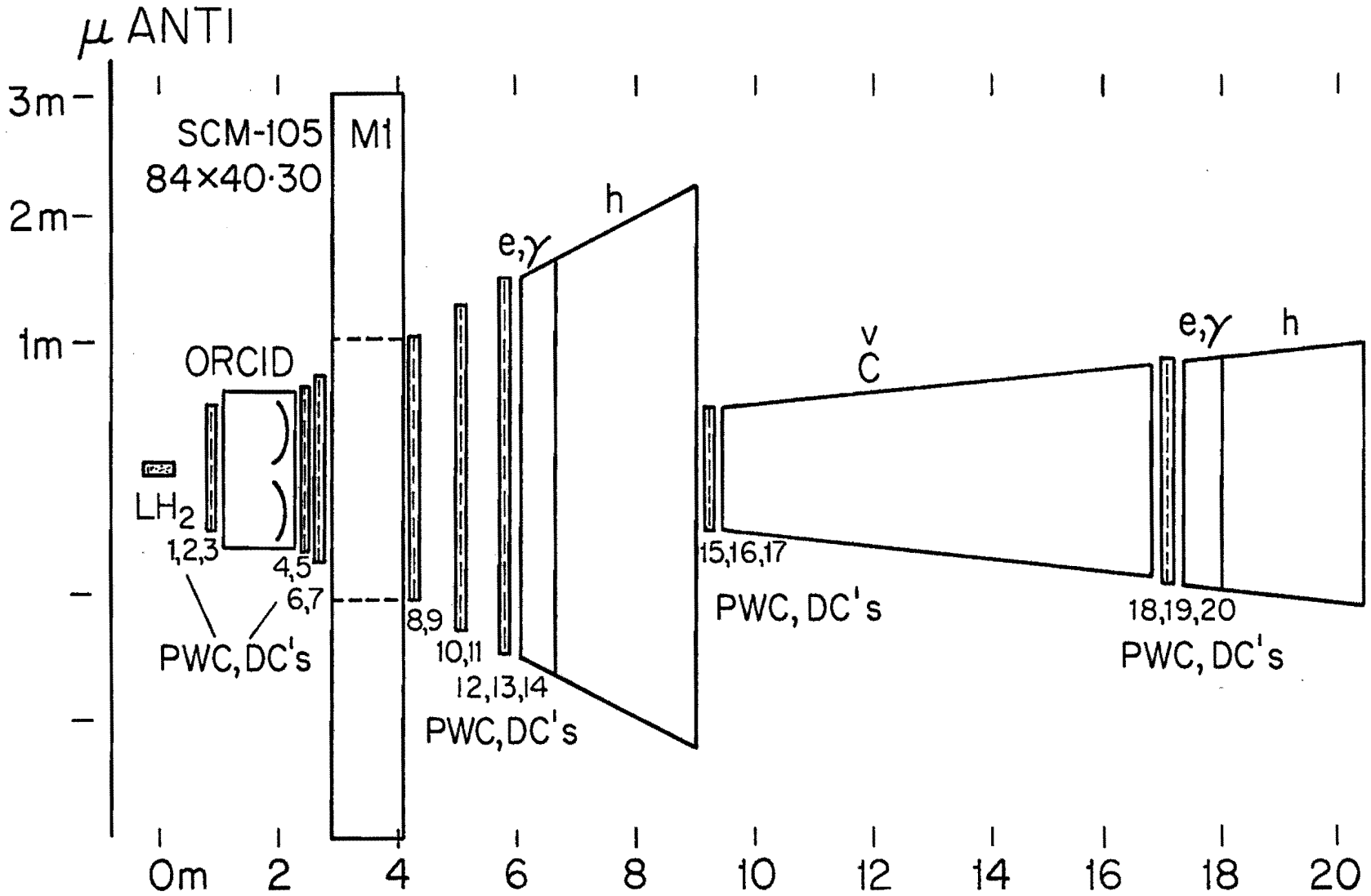
μ ANTI
3m
2m
1m
SCM-105
84×40·30
M1
ORCID
LH2
1,2,3
4,5
6,7
PWC, DC's
8,9
10,11
12,13,14
PWC, DC's
e,γ
h
15,16,17
PWC, DC's
v
C
e,γ
h
18,19,20
PWC, DC's
0m
2
4
6
8
10
12
14
16
18
20

Figure 4.1

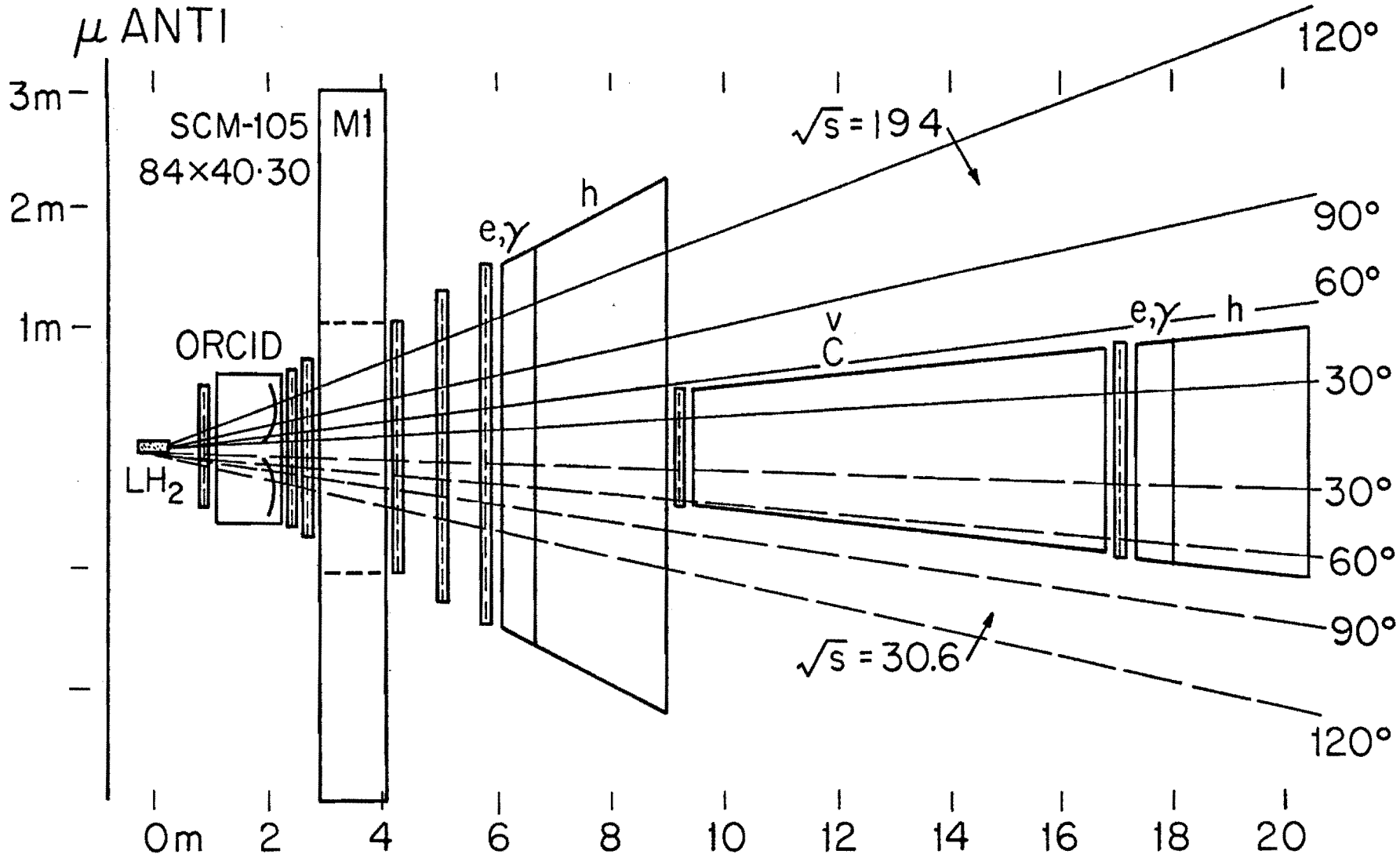
μ ANTI
3m
2m
1m
SCM-105
84×40·30
M1
ORCID
LH2
e,γ
h
√s = 19.4
120°
90°
60°
30°
30°
60°
90°
120°
e,γ
h
C
v
√s = 30.6
0m
2
4
6
8
10
12
14
16
18
20

Figure 4.2

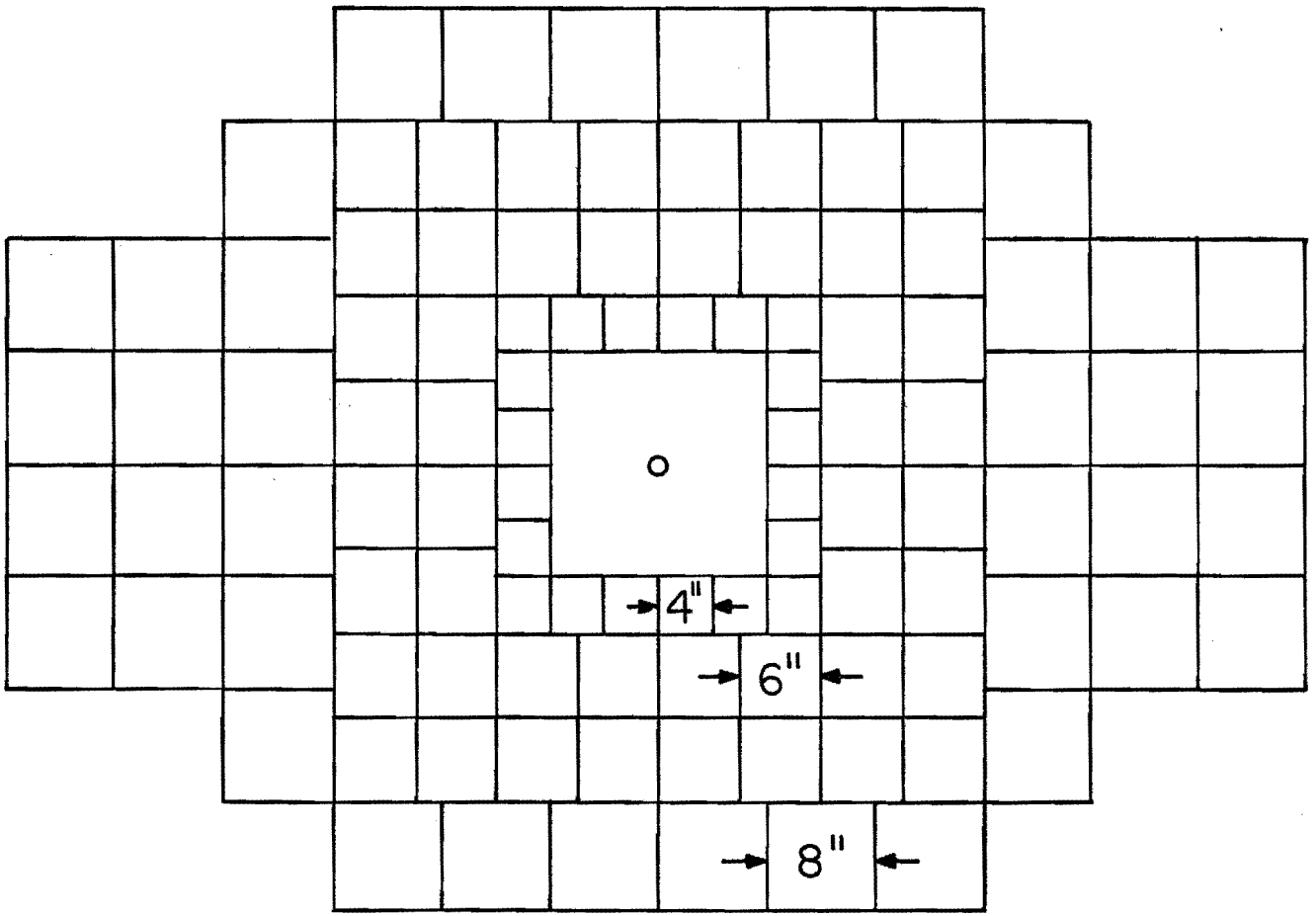

Figure 4.3

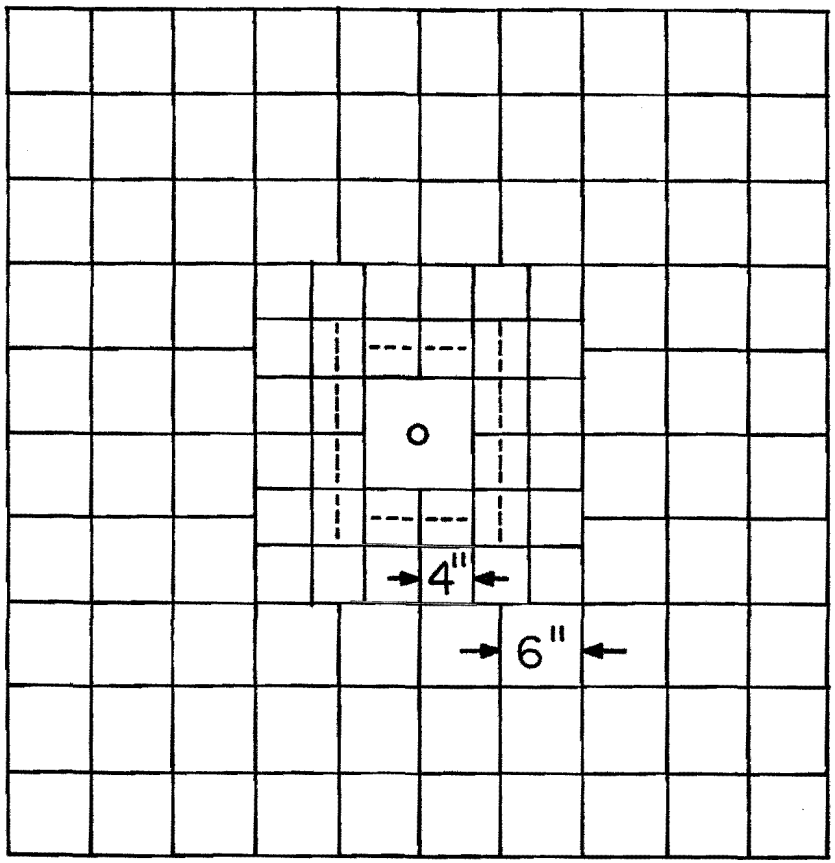

Figure 4.4

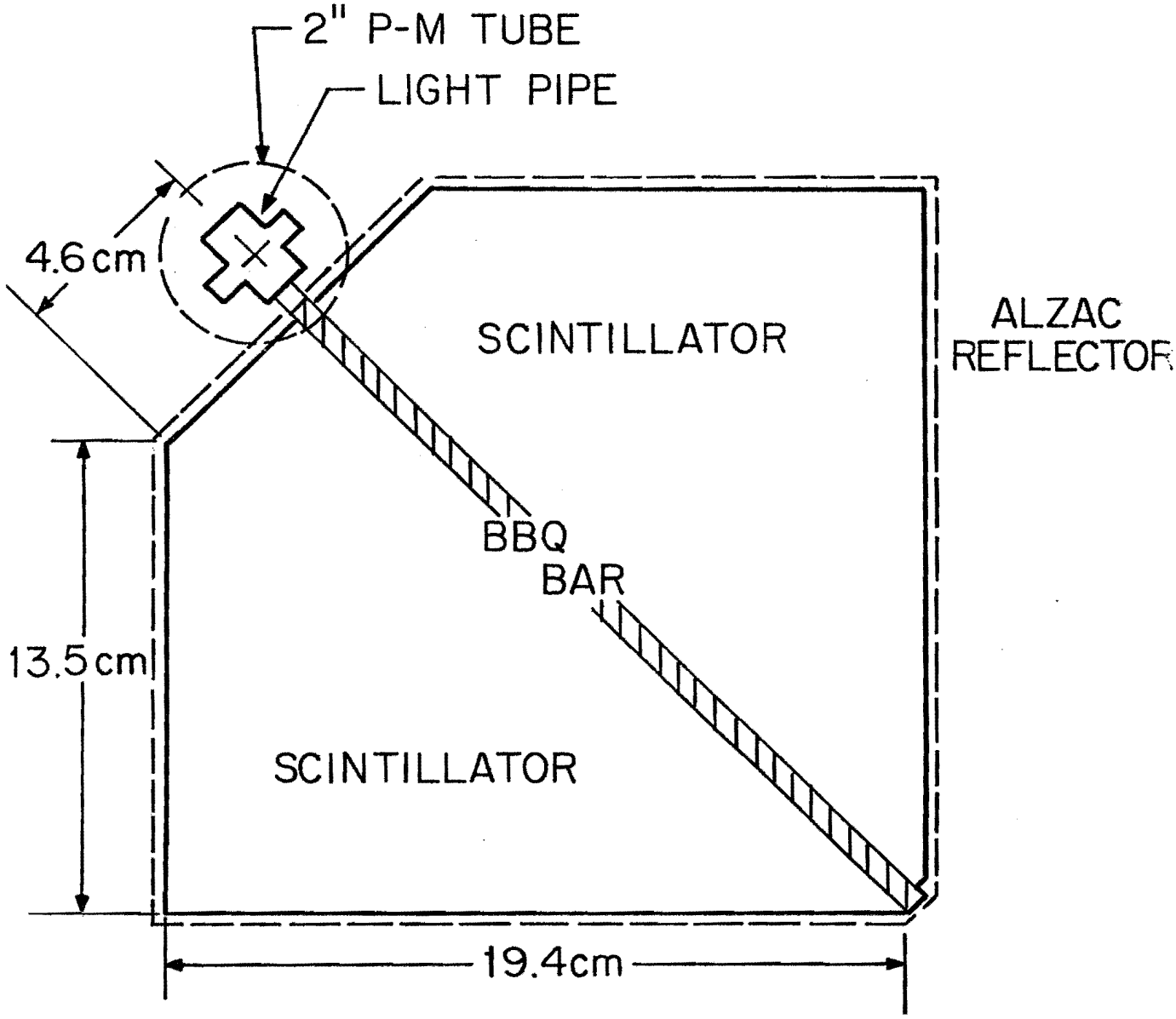
2" P-M TUBE
LIGHT PIPE
4.6 cm
SCINTILLATOR
ALZAC
REFLECTOR
BBQ
BAR
13.5 cm
SCINTILLATOR
19.4cm

Figure 4.5

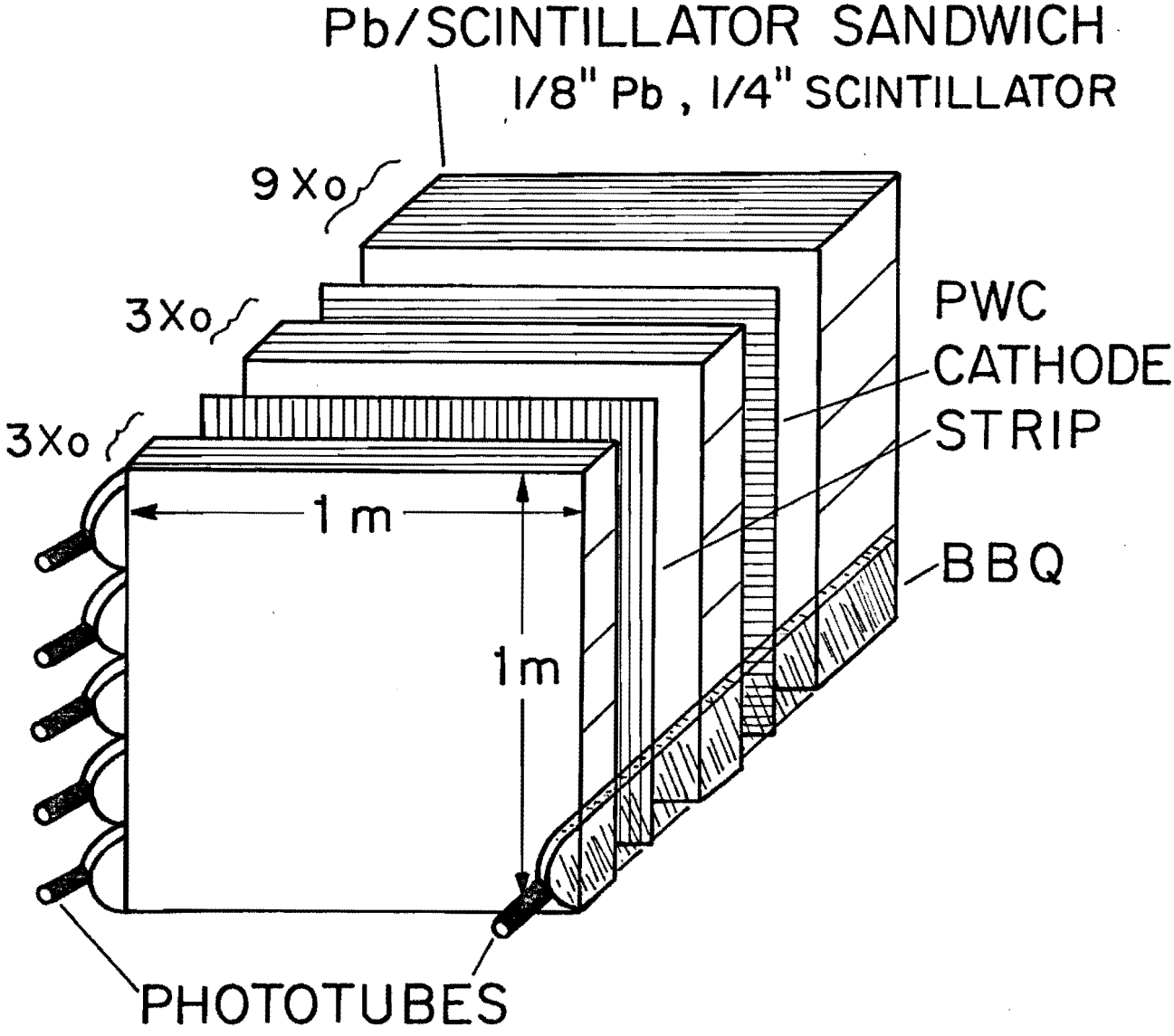
Pb/SCINTILLATOR SANDWICH
1/8" Pb , 1/4" SCINTILLATOR
9 Xo
3Xo
3Xo
PWC
CATHODE
STRIP
BBQ
1 m
1m
PHOTOTUBES

Figure 4.6

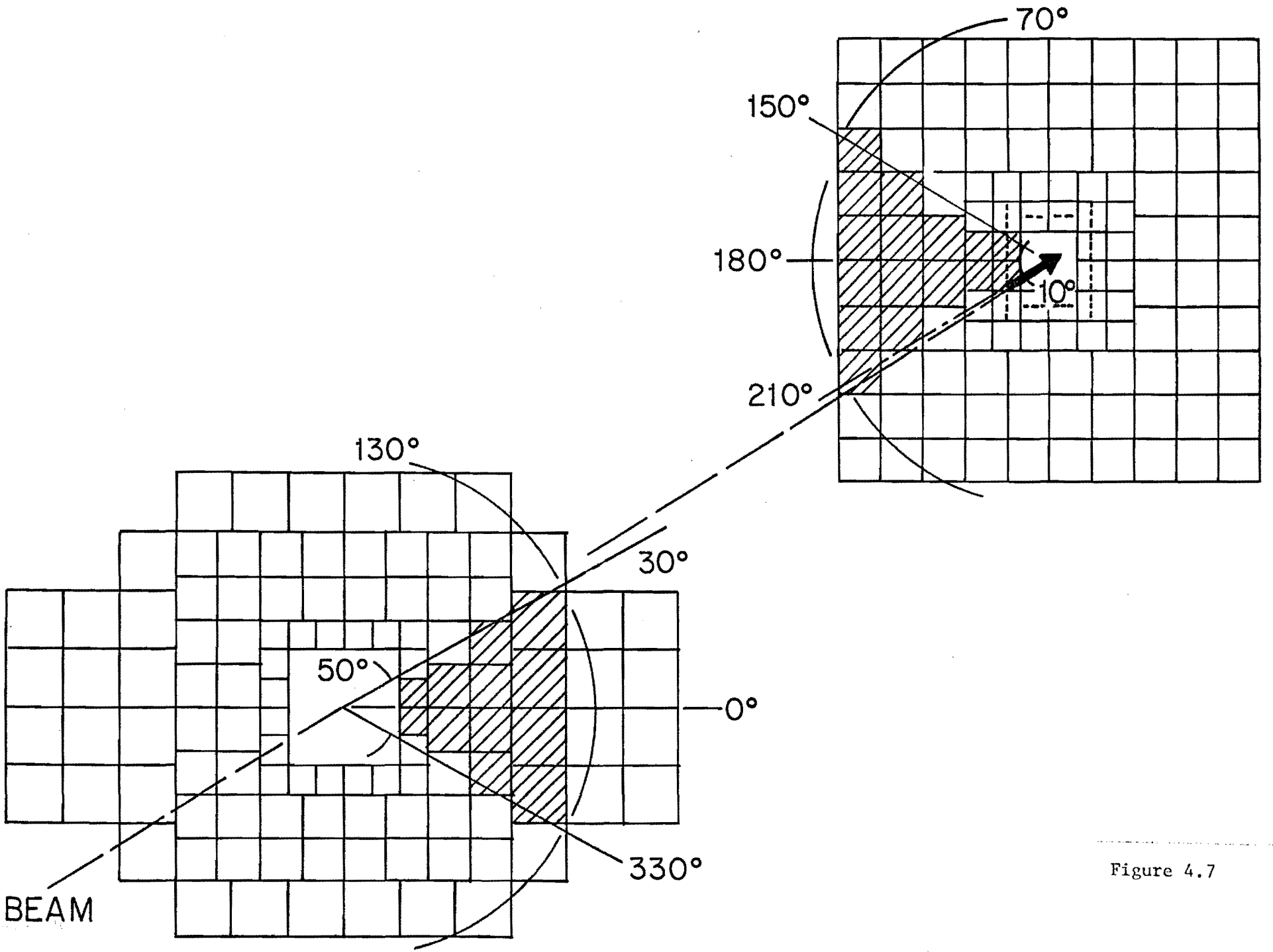

Figure 4.7

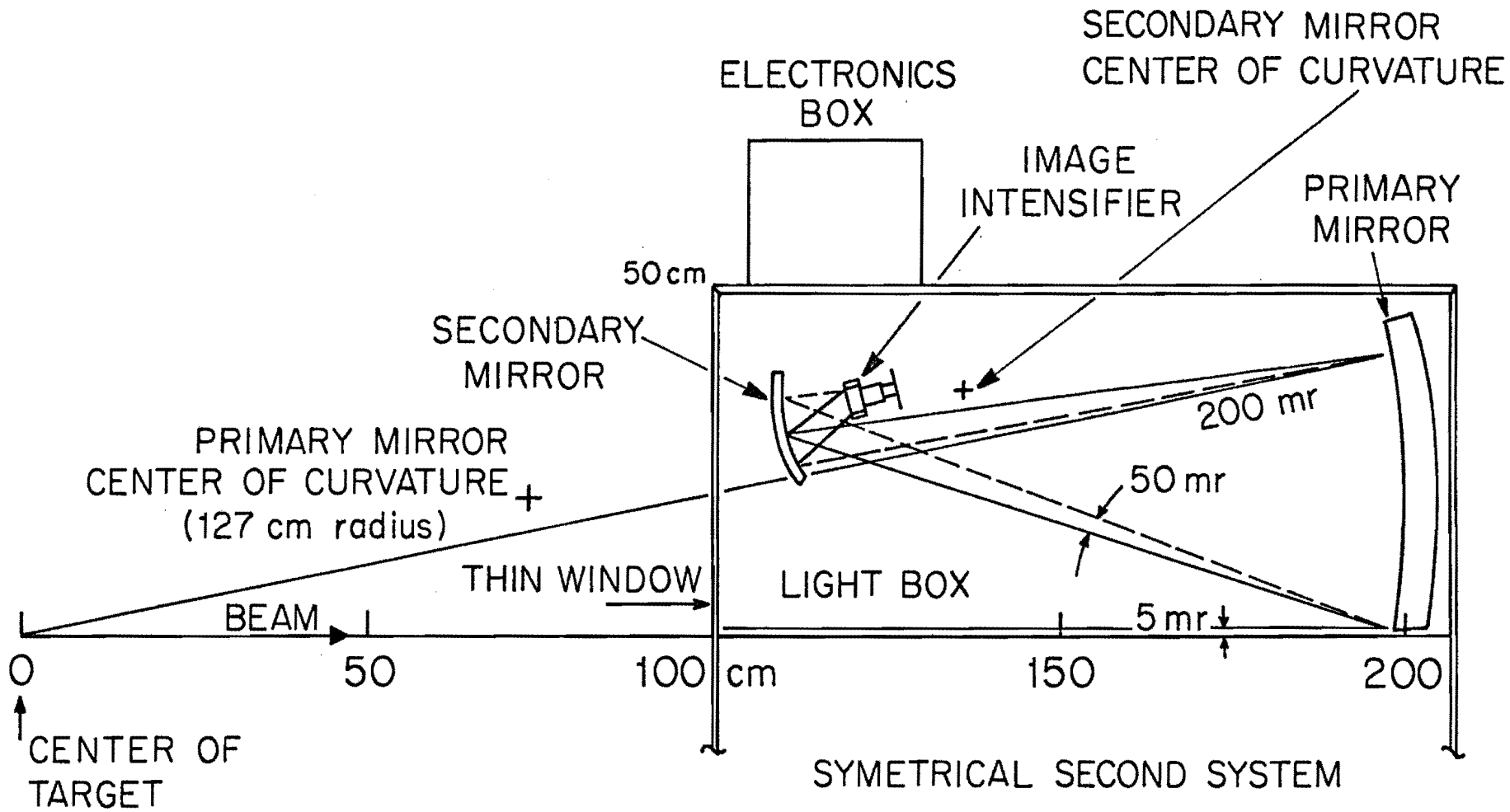
TWO - MIRROR ORC ID LAYOUT
(PRELIMINARY)
SECONDARY MIRROR
CENTER OF CURVATURE
ELECTRONICS
BOX
IMAGE
INTENSIFIER
PRIMARY
MIRROR
50 cm
SECONDARY
MIRROR
200 mr
PRIMARY MIRROR
CENTER OF CURVATURE
(127 cm radius)
50 mr
THIN WINDOW
LIGHT BOX
BEAM
5 mr
0
50
100
cm
150
200
CENTER OF
TARGET
SYMETRICAL SECOND SYSTEM

Figure 4.8

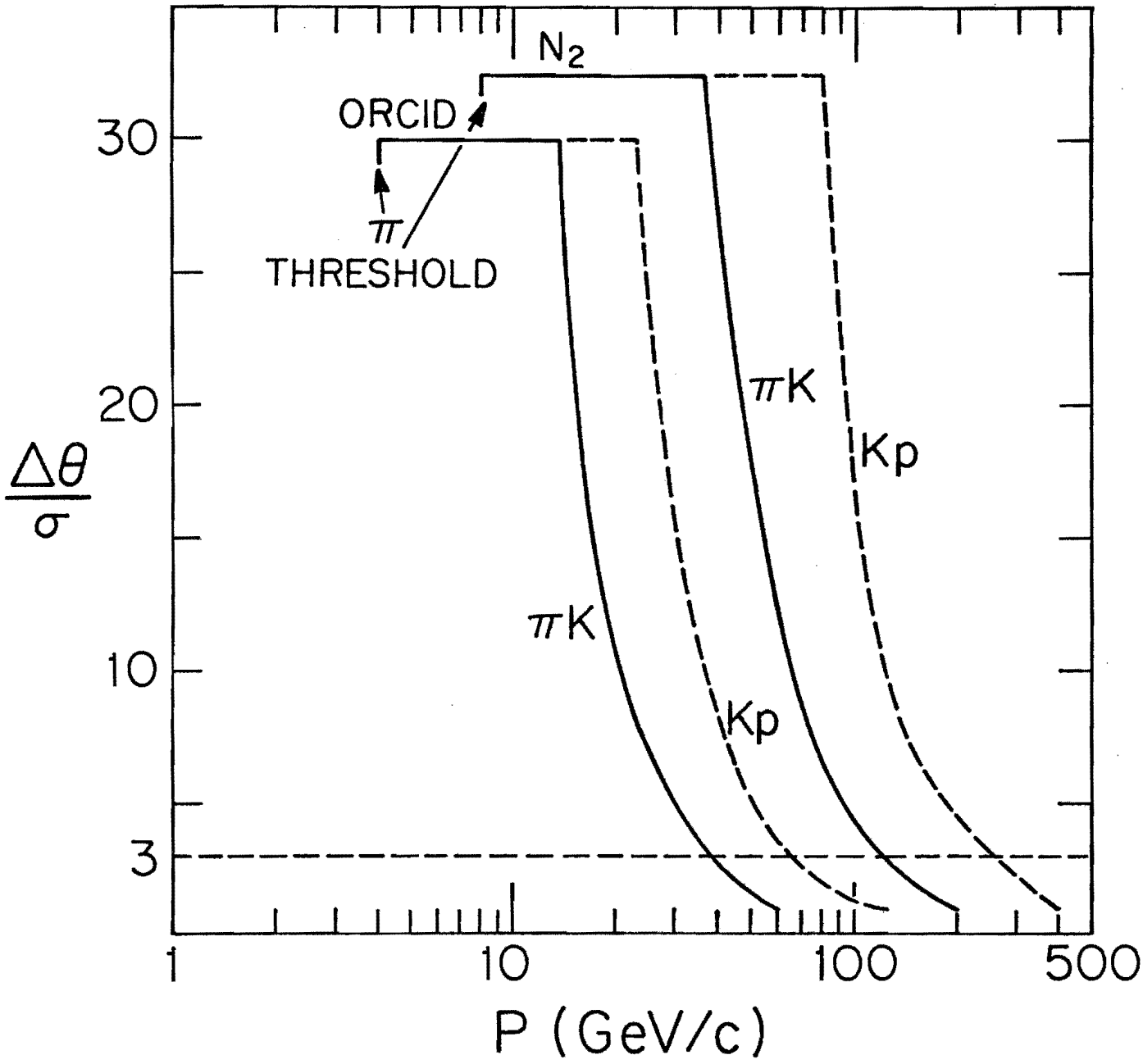

Figure 4.9

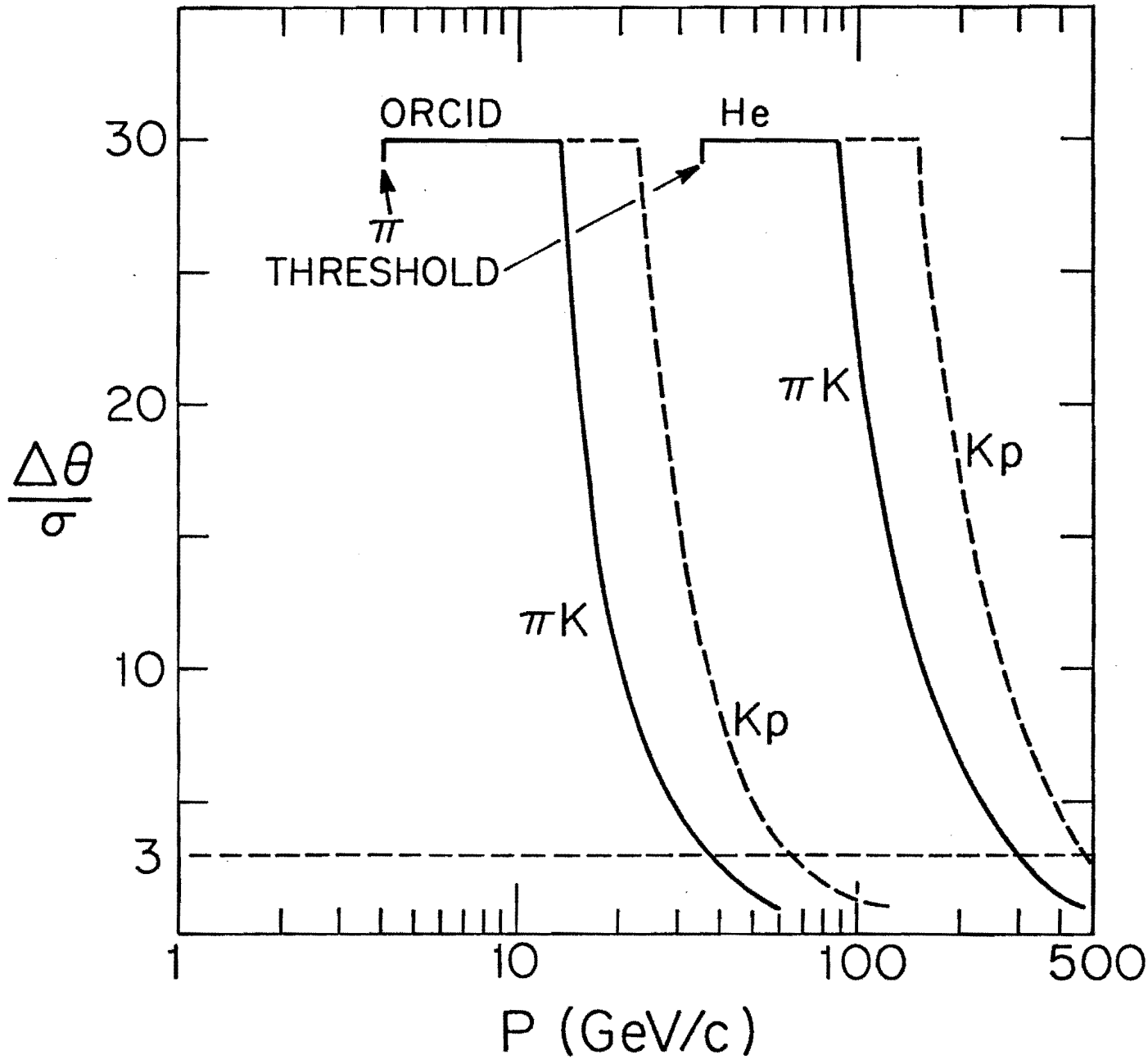
ORCID
He
30
20
10
3
π
THRESHOLD
πK
Kp
πK
Kp
$\frac{\Delta\theta}{\sigma}$
1
10
100
500
P (GeV/c)

Figure 4.10